Temperature-dependent thermal transport properties of carbonate minerals and rocks

Jesse D. Merriman[1],*, Anne M. Hofmeister[2],*, Derick J. Roy[2],*, and Alan G. Whittington[1],*
[1]Department of Geological Sciences, The University of Missouri, Columbia, Missouri 65211, USA
[2]Department of Earth and Planetary Sciences, Washington University, St. Louis, Missouri 63130, USA

ABSTRACT

To address thermal processes involving carbonate rocks, we measured thermal diffusivity (D) of a suite of carbonate minerals and rocks using laser flash analysis at temperatures from ~300 K up to ~1000 K. For different minerals, D was governed by density or unit cell size. Near room temperature, for example, D ranged from 4.36 mm^2 s^{-1} for magnesite to 1.61 mm^2 s^{-1} for calcite. At any given temperature, D decreases from magnesite to dolomite to rhodochrosite to calcite. As temperature increases, D decreases for all samples, with the strongest drop occurring in the interval ~300–500 K. For rocks, mineralogy and porosity were also strong controls on rock D. Calcitic limestones showed proportionally lower D than the mineral, scaling with measured pore fraction, whereas dolomitized rocks produced higher D than calcitic rocks across the interval 300–600 K. Measurements of heat capacity and density were used to calculate thermal conductivity (k) for the suite, and these results show a stronger temperature dependence for k of carbonate rocks and minerals than previous studies, with k decreasing by ~50% between ambient and ~600 K.

These results can strongly affect models of the geothermal gradient. Because dolomite conducts heat more efficiently across all measured temperatures than calcite, regions with large proportions of dolomitized rocks may have lower temperatures at depth than those dominated by calcitic carbonates. Additionally, the strong temperature dependence of carbonate rocks introduces the potential for feedback relationships in high heat–producing or thin crust, suggesting that carbonate-dominated crust could have higher temperatures at depth than previously thought. This strong temperature dependence also has implications for the duration of metamorphic events such as metasomatism driving skarn mineralization, or contact metamorphism resulting from intrusion of an igneous body.

■ INTRODUCTION

Carbonate rocks are a significant component of the upper continental crust (Ronov and Yaroshevsky, 1976; Rudnick and Gao, 2003), and thus their thermal transport properties—thermal conductivity (k) and thermal diffusivity (D)—

*E-mail: jdm42c@mail.missouri.edu (Merriman), hofmeist@wustl.edu, derick.roy@wustl.edu, whittingtona@missouri.edu

influence important processes such as hydrocarbon maturation and the carbon cycle, in addition to geodynamic processes and geothermal energy potential (e.g., Bickle, 1996; Berner and Caldeira, 1997; Schütz et al., 2012). Because carbonate rocks blanket many platform regions of continental interiors, their role in moderating continental heat flow is potentially important, as thermal conductivity varies more at the low temperatures associated with shallow depths than at the high temperatures commonly found in the deeper interior (Whittington et al., 2009; Nabelek et al., 2010; Liu et al., 2011; Merriman et al., 2013). Despite the ubiquitous occurrence of carbonates, little is known about the effects of mineralogy and texture on their thermal properties above ambient temperatures. The remainder of this section briefly reviews heat transfer and methods for measuring the thermal transport properties of rocks and minerals to high temperature.

Thermal conductivity is the product of density (ρ), heat capacity (C_P), and thermal diffusivity:

$$k = \rho C_P D. \tag{1}$$

All of the above properties vary as functions of temperature (T) and, to a lesser extent, pressure (P) (reviewed by Hofmeister, 2007; Hofmeister et al., 2007). In the range of ~300–600 K, negative dD/dT dominates over positive dC_P/dT in rocks, and, because changes in ρ are relatively small, k decreases as temperature increases. Variations in k with temperature can be large, because D can decrease by as much as a factor of 10 for crustal rocks (e.g., Merriman et al., 2013; Hofmeister and Branlund, 2015), while C_P typically increases by no more than a factor of two (e.g., Robie and Hemingway, 1995; Waples and Waples, 2004). The decrease in D and k as T increases beyond ambient temperature is a consequence of stimulation of additional lattice vibrations as T increases. More interactions occur as T climbs, and so the mean free path decreases and so does D. In general, the mean free path is considered inversely dependent upon T (see Hofmeister and Branlund [2015] for a review of the relevant literature).

Furthermore, decreases in ρ with increasing T are small because thermal expansivity of crystals is low, typically ~1–3 × 10^{-5} K^{-1} (Fei, 1995), and in the crust is offset by increasing P with depth. Elevated P typically increases D, but again the effect is small, on the order of 3%–5% per gigapascal (Hofmeister, 2007; Hofmeister and Pertermann, 2008). This increase in D with increasing P

is primarily a result of increasing density, and these effects are negligible compared to those resulting from variations in mineralogy (Hofmeister et al., 2007).

Many experimental methods used to measure *k*, such as the divided bar method, produce systematic errors (see Hofmeister et al., 2007). Physical contacts between the heat source and the sample are imperfect on a microscopic scale, leading to underestimates of *k* by ~10% per contact. In addition, radiative transfer can occur between the heat source and the sensor without interaction with the sample, resulting in measurements of *k* that are artificially elevated (Mehling et al., 1998). This "ballistic" radiative transfer is an artifact of the experimental method and is not found in natural settings (Hofmeister, 2010).

Contamination of measurements with spurious radiative transfer commonly goes unrecognized because the process is not well understood. Infrared spectroscopic data provide some insights. The effect of ballistic radiative transfer is strongest in minerals that are transparent in the near infrared (near IR) (Fig. 1). Although mineral transparency changes with temperature, many common rock-forming minerals are partially or fully transparent across the
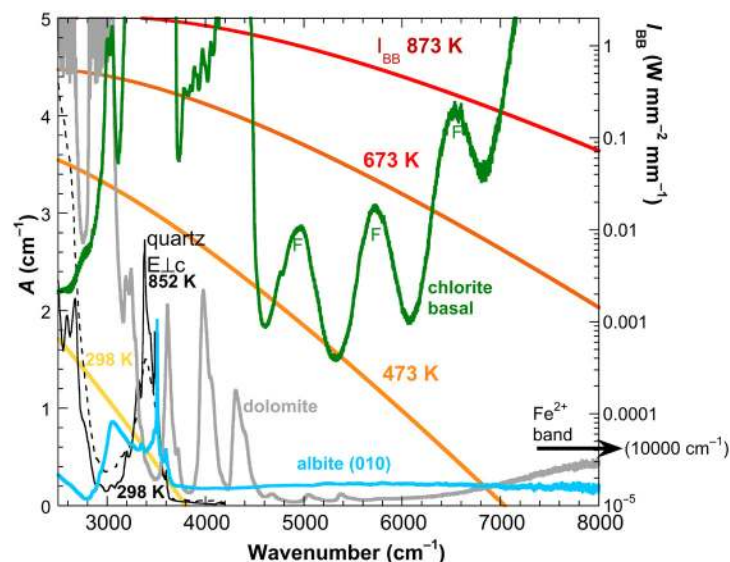

Figure 1. Comparison of near-infrared absorption spectra to ideal emissions of a blackbody for various minerals (warm colors, as labeled on a logarithmic scale). *A* is the absorption coefficient and is defined as absorbance/sample thickness. Black lines are for quartz at room (solid line) and elevated (dashed line) temperature. E⊥c indicates that light polarized along the *c*-axis, from Aines and Rossman (1985); sample thickness was not reported, but is estimated to be ~1 mm. Grey line is for a dolomite cleavage from a 6.73 mm sample with grey coloration. Blue line is for albite (variety cleavelandite) from a 4.8 mm cleavage. Green line is for chlorite (variety penninite) from a 0.25 mm basal flake. "F" indicates interference fringes due to internal layers, which contribute reflections and artificially high absorption coefficients. Bands for OH are off the scale. The rise of the dolomite and chlorite spectral curves as frequency increases is due to d-d electronic transitions of Fe^{2+} near 10,000 cm^{-1} (which occurs outside the scale of this graph).

range of temperatures at which they are stable. Minerals with high concentrations of water or hydroxyl and high concentrations of Fe^{2+} in large sites are the only types that strongly absorb in this spectral region (Rossman, 1988a, 1988b). Because heat transfer data are typically collected on ~3–5 mm thicknesses (note in Fig. 1 that absorbance (*A*) is calculated from $A = -\log(I_{trans}/I_0)$, where I_{trans} is the intensity of the transmitted light, and I_0 is the intensity of the incident light on the sample). A = 1 describes optically thin conditions for a 1 cm sample. Light crosses typical sedimentary minerals with little attenuation in the near-IR region. Division by the measured thickness provides the absorption coefficient. Both effects reduce throughout. Near room temperature, the effect is small, resulting in scatter in measured values. At high *T*, however, ballistic transport results in excessive *D*, and sometimes in an incorrect sign for the temperature derivative, mostly because intensity of blackbody radiation grows as T^3. In rocks, scattering along grain boundaries limits this effect, but at the expense of reducing *D* or *k* due to thermal grain boundary resistance (Smith et al., 2003). These competing effects create a roughly correct answer for *D* or *k* near room *T*, but with substantial uncertainties.

Because the common sedimentary minerals quartz and feldspar are transparent in the near IR (Fig. 1), experimental methods for the measurement of *k* of these minerals (and rocks dominated by them) are susceptible to ballistic radiative transfer, particularly above ambient *T* (Branlund and Hofmeister, 2007). In the laser flash analysis (LFA) method, first developed by Parker et al. (1961), the effects of ballistic radiative transfer can be removed from the time-*T* curve using the model of Mehling et al. (1998). The model fit is shown in Figure 2. Furthermore, this method avoids physical contact between the heat source and sample, eliminating this error source and thus isolating diffusive heat transfer.

Consequently, the LFA method produces results for thermal diffusivity (*D*) with errors of ±5% at room temperature and ±<2% at elevated temperatures (Hofmeister, 2006). The effect of removing radiative transfer in quartz and the feldspars has been well documented (Branlund and Hofmeister, 2007, 2008, 2012; Pertermann et al., 2008; Hofmeister et al., 2009). Both show decreasing *D* as temperature rises above ambient (Branlund and Hofmeister, 2007; Pertermann et al., 2008; Hofmeister et al., 2009), although *dD*/*dT* is much higher for quartz than for the feldspars. This pattern extends to quartz- and feldspar-dominated rocks (e.g., Whittington et al., 2009; Miao et al., 2014), although other properties such as porosity (φ) and pore contents become important (Branlund and Hofmeister, 2008).

The dominant minerals in carbonate rocks, calcite ($CaCO_3$) and dolomite [$CaMg(CO_3)_2$], have not been examined using LFA. Note that we use the naming convention "dolomite" for the mineral, and "dolomite rock" for the sedimentary rock to avoid confusion, as both the mineral and rock appear in several of the same figures. Measurements of *k* of both minerals exist in the literature (e.g., Birch and Clark, 1940; Horai, 1971), but these historical studies covered a limited temperature range and used methods that were subject to the experimental errors discussed above. More recently, *D* of calcite was measured using a photoacoustic spectroscopic method (Ramachandran et al., 2006), but only at room temperature. Thermal diffusivity data for a suite of 11
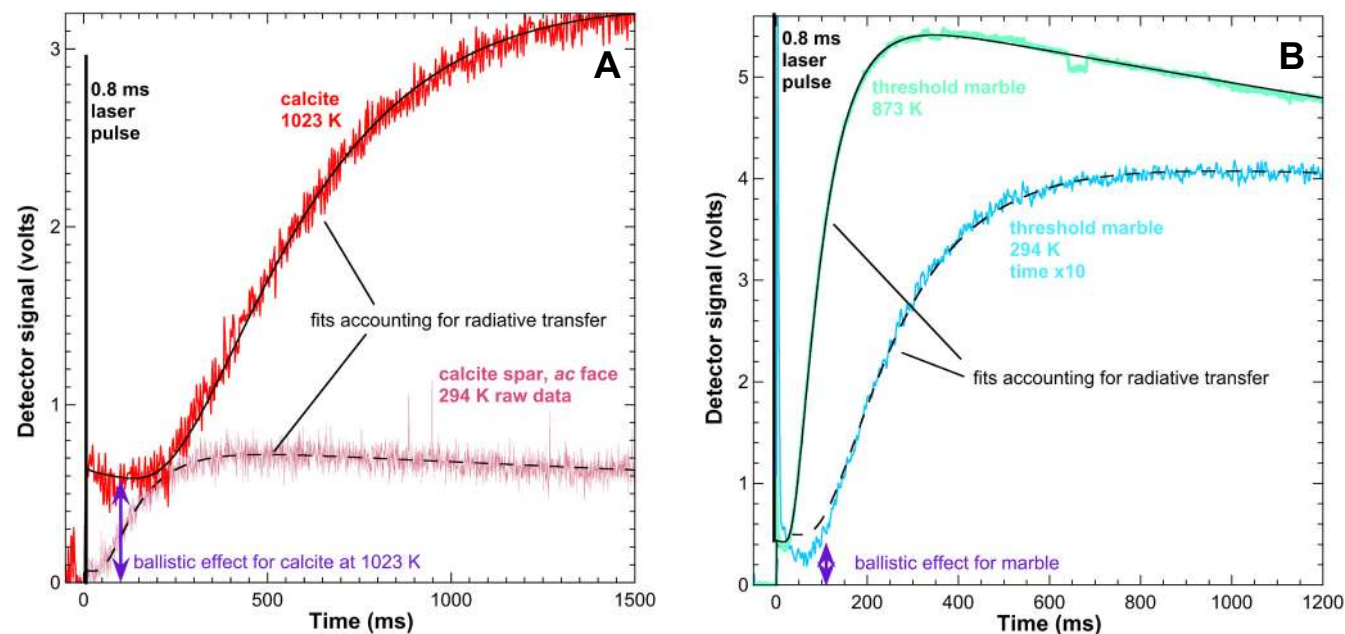
Figure 2. Time-temperature curves for single-crystal and grainy calcite samples. Colored curves show raw data for temperatures and samples as labeled; black curves show the model of Mehling et al. (1998). (A) Single-crystal calcite. Double purple arrow shows immediate jump in intensity following the firing of the laser at time $t = 0$ ms for the calcite at high temperature (T). The jump at room T is small for the calcite, but non-negligible. (B) Threshold marble. Despite the fine grain size, the radiative response exists, but depends weakly on temperature due to mitigation by scattering. Similar results have been found for other minerals (e.g., quartz; Branlund and Hofmeister, 2007). Note that the curve for "threshold marble 294 K" is compressed along the time axis by a factor of 10 to fit both curves on the same graph, and values should be multiplied by 10.

carbonate minerals were collected across a wide range of temperatures using a modified transient technique (Gratz, 2006), but this method does not fully control radiative transfer and involves one physical contact which artificially reduces D (Hofmeister et al., 2007). Similar to quartz and feldspar, absorption spectra of these minerals in the near IR show a strong potential for spurious radiative transfer in experiments (Fig. 1).

Moreover, there is a paucity of high-temperature D and k data for carbonate minerals and rocks, which can have widely varying textures and porosity depending on their mode of formation and degree of diagenesis or metamorphism. Although the mineralogy of limestones is relatively simple, considerable variety arises from packing of different biological detritus of highly variable shape and size, and, combined with chemical precipitation of calcite, leads to a spectrum of textural variation. Furthermore, recrystallization can occur at various stages of maturity post-diagenesis, with fossils acting as nucleation points or centers of replacement (Lippmann, 1973). Consequently, φ in carbonate rocks varies widely. At near-surface P, calcitic limestone generally has higher φ than dolomite rock, but the reverse is true when $P > \sim$50 MPa in natural settings (Hantschel and Kauerauf, 2009).

Many workers have proposed models for the prediction of the temperature response of k of rocks using measurements at room T (Clauser and Huenges, 1995; Lee and Deming, 1998). These are based on results from contact methods, however, and do not incorporate mineralogical differences. Lee and Deming (1998) reviewed five such models for T-dependent k based on single room-T measurements of k. However, demonstrably more complex behavior occurs in minerals than can be captured by a single equation for different minerals, an observation that extends to measurements of rocks composed of more than one mineral (Whittington et al., 2009; Merriman et al., 2013), and thus a single equation is unlikely to reproduce the range of observed changes in thermal transport properties with T across all rock types

We present new D data on calcite, dolomite, magnesite ($MgCO_3$), and rhodochrosite ($MnCO_3$), and a suite of carbonate rocks, measured using the LFA method. We also measured ambient ρ and the temperature dependence of C_P, from which we calculate k as a function of T. We test existing models and explore the effects of porosity on the T-dependent thermal transport properties of these important rocks.

| TABLE S1. EPMA DETECTION LIMITS, CALCULATED ERROR, AND CALIBRATION STANDARDS | | | | | | | | | | |
Si CDL	Al CDL	Fe CDL	Mn CDL	Mg CDL	Ca CDL	Na CDL	K CDL	S CDL	Ti CDL	Cr CDL
Minerals										
Calcite Spar	0.0134	0.0106	0.0279	0.0271	0.0115	0.0122	0.0187	0.0085	–	0.0156	0.0158
Calcite Spar	0.0133	0.0105	0.0268	0.0280	0.0114	0.0119	0.0186	0.0088	–	0.0167	0.0156
Calcite Spar	0.0131	0.0104	0.0259	0.0257	0.0113	0.0120	0.0192	0.0082	–	0.0159	0.0161
Calcite Spar	0.0131	0.0107	0.0279	0.0289	0.0112	0.0117	0.0179	0.0087	–	0.0162	0.0156
White Dolomite	0.0128	0.0104	0.0249	0.0244	0.0107	0.0108	0.0170	0.0089	–	0.0148	0.0145
White Dolomite	0.0127	0.0104	0.0243	0.0248	0.0106	0.0106	0.0167	0.0094	–	0.0149	0.0146
White Dolomite	0.0127	0.0103	0.0250	0.0285	0.0106	0.0110	0.0166	0.0092	–	0.0144	0.0144
White Dolomite	0.0127	0.0104	0.0250	0.0243	0.0106	0.0104	0.0162	0.0088	–	0.0143	0.0144
Grey Dolomite	0.0114	0.0092	0.0102	0.0093	0.0094	0.0093	0.0134	0.0059	0.0030	–	–
Grey Dolomite	0.0114	0.0092	0.0103	0.0094	0.0095	0.0093	0.0136	0.0059	0.0030	–	–
Magnesite	0.0111	0.0088	0.0096	0.0085	0.0086	0.0065	0.0113	0.0061	0.0029	–	–
Magnesite	0.0111	0.0088	0.0096	0.0085	0.0086	0.0065	0.0113	0.0060	0.0028	–	–
Magnesite	0.0111	0.0088	0.0095	0.0085	0.0085	0.0065	0.0113	0.0060	0.0028	–	–
Rhodochrosite	0.0130	0.0113	0.0116	0.0110	0.0124	0.0075	0.0207	0.0069	0.0034	–	–
Rhodochrosite	0.0130	0.0113	0.0116	0.0110	0.0124	0.0075	0.0206	0.0069	0.0034	–	–
Rhodochrosite	0.0130	0.0112	0.0116	0.0110	0.0123	0.0075	0.0206	0.0069	0.0034	–	–

■ EXPERIMENTAL METHODS

Sample Selection

Four different species of carbonate minerals were studied (Table 1), including two calcite samples (calcite spar and hexagonal calcite [calcite hex], both from the collection of the Department of Earth and Planetary Sciences at Washington University, St. Louis, Missouri, USA), a dolomite sample with both white and grey ends (white dolomite and grey dolomite, from Eugul, Navarre, Spain), magnesite (from Brumado, Bahia, Brazil), and rhodochrosite (from Wudong Mine, Wushuo Prefecture, Guangxi Zhuang, China). Magnesite was included to provide data on the Mg-bearing layers of dolomite. The addition of rhodochrosite permits examination of the effect of cation mass on mineral D. Rock samples include four calcite-dominated limestones from central Missouri: TF-001, a fossiliferous limestone from the Winterset Limestone; TF-002, an oolitic limestone from the Drum Limestone; MO-05, a boundstone from the Burlington Limestone; and MO-07, a micrite from the University of Missouri departmental collection. Additional rocks include: sample KS-002, a sedimentary dolomite rock from the Jefferson City Dolomite (Missouri), four calcite-dominated marbles, samples of Threshold marble (a building stone from a commercial retailer, Lowes, in Maplewood, Missouri, USA), Black marble (also from a commercial retailer, The Tile Store, in St. Anne, Missouri, USA), and Carrara Marble (Italy), including a marble deformed at ambient temperature under triaxial loading (Carrara deformed); sample AW-05, a marble with mixed calcite and dolomite phases (from Ross Lake near North Cascades National Park, Washington, USA); sample 17-4, a dolomitic marble (from the Eureka Valley–Joshua Flat–Beer Creek [EJB] aureole, White Mountains, California, USA; Nabelek and Morgan, 2012); sample 33-1, a forsterite- and chlorite-bearing calcite-dolomite marble (also from the EJB aureole); and a magnesite conglomerate (from the departmental collection at Washington University). The suite of rocks permits exploring effects of (1) depositional environments ranging from intertidal to shallow marine; (2) dolomitization; (3) porosities; and (4) contact and burial metamorphism involving variable mineralogy. We used polarized-light microscopy to describe mineralogy and textures and to measure grain sizes.

X-Ray Diffraction

Mineral proportions were determined using a Bruker D8 ADVANCE X-ray diffractometer (XRD). Weight-percent proportions were calculated from diffraction patterns with the Bruker software TOPAS (version 5), using the refinement method of Rietveld (1968). Results were converted to volume percent using published values of density for minerals (Deer et al., 1992), and using microprobe data to calculate end-member proportions of solid-solution minerals such as olivine.

Electron Microprobe

Mineral compositions were analyzed by wavelength-dispersive analysis with a JEOL JXA-8200 electron microprobe, and using Probe for Windows software for data reduction (Probe Software, Inc., Eugene, Oregon, USA; http://www.probesoftware.com/). The measured data were corrected with CITZAF software after Armstrong (1995). Oxide and silicate standards were used for calibration: Amelia albite for Na and Si; microcline for K; Gates wollastonite for Ca; Alaska anorthite for Al; synthetic fayalite for Fe; synthetic forsterite for Mg; synthetic TiO_2 for Ti; synthetic Mn-olivine for Mn; and synthetic Cr_2O_3 for Cr. Detection limits, calculated error, and calibration standards are available in Table S1[1].

Chemical Analysis

Chemical analysis of rock samples was performed on limestones TF-001, TF-002, MO-05, MO-07, and KS-002 and marbles 33-1, 17-4, and Black marble by Activation Laboratories, Inc. (Ontario, Canada), using inductively coupled plasma–optical emission spectroscopy (ICP-OES) on lithium metaborate fusions for major oxide analysis, and combustion spectroscopy for total carbon and graphitic carbon analysis (through combustion and binding of carbon with oxygen to form CO and CO_2). Calibration standards and duplicate measurements are available in Table S2 [footnote 1].

Infrared Spectroscopy

We used an evacuated Bomem DA3.02 Fourier transform interferometer with an SiC source, an InSb detector, and a CaF_2 beamsplitter for IR spectroscopy. Instrumental accuracy is 0.01 cm^{-1}. About 1000 scans were collected at room temperature from ~1200 to 5000 cm^{-1} at a resolution of 2 cm^{-1}. Data were collected from samples mounted on an ~1 mm aperture, which served as the reference.

Density

Density was measured using three different methods. (1) Bulk density was determined using a geometric method, where the sample was cut into a regular shape (cube or cylinder) and then measured with a micrometer, and weighed on an analytical balance. Longer cores (1–3 cm) were used to reduce errors associated with imperfections. Uncertainties are estimated at 2% based on variability between different cores of the same sample. (2) Density of the solid and its isolated pore spaces was ascertained using the Archimedean method. Samples were weighed in air and again while immersed in fluid (ethanol). The sample was soaked overnight to enable fluid penetration through-

TABLE 1. SAMPLE CHARACTERISTICS

Rocks	Source	Average grain size (mm)	LFA sample thickness (mm)	Mineralogy (wt%)	Geometric density (g cm⁻³)	Archimedean density (g cm⁻³)	Skeletal density (g cm⁻³)	Porosity (%)
TF-001	Winterset Limestone, Missouri, USA	0.007	1.36	cc: 97.2 qtz: 2.8	2.46	2.67	2.71	9
TF-002	Drum Limestone, Missouri, USA	0.005	1.43	cc: 93.8 qtz: 6.2	2.34	2.67	2.71	13
MO-05	Burlington Limestone, Missouri, USA	0.034	1.26	cc: 98.2 dol: 1.3 qtz: 0.5	2.55	2.64	2.71	6
MO-07	Departmental collection, University of Missouri, Department of Geological Sciences	0.005	1.00	cc: 99.8 qtz: 0.2	2.66	2.68	2.71	2
KS-002	Jefferson City Dolomite, Missouri, USA	0.031	1.22	dol: 79.0 kfs: 11.4 qtz: 9.6	2.38	2.77	2.79	15
Carrara Marble	Carrara Marble, Italy	0.062	disk 1 - 1.46 disk 2 - 1.64 disk 3 - 1.73 disk 3, run 2 - 1.62 disk 3, run 3 - 1.52 trapezoid - 1.52	cc: 100	2.61	2.66	2.72	4
Carrara Marble (deformed)	Carrara Marble deformed under triaxial loading	0.006	0.84	cc: 100	2.29	n/a	2.72	16
Threshold marble	Commercial building stone, Home Depot	0.081	0.50	cc: 100	2.6	n/a	2.72	4
Black marble	Commercial building stone, Home Depot	0.044	0.70	cc: 99.1 qtz: 0.9	2.61	n/a	2.71	4
33-1	EJB aureole, White Mountains, California, USA	0.095	white II - 0.79 white LI - 1.06	cc: 58.5 chl: 15.2 dol: 10.3 for: 16.0	2.84	2.82	2.82	<1
17-4	EJB aureole, White Mountains, California, USA	0.369	white II - 1.03 white LI - 1.11 grey II - 1.01 grey LI - 0.92	dol: 94.1 cc: 5.8	2.84	2.76	2.83	<1
AW-05	Ross Lake, near North Cascades National Park, Washington, USA	0.7	1.44	cc: 56.4 dol: 37.0 chl: 6.6	2.74	2.73	2.76	<1
Magnesite conglomerate	Departmental collection, Washington University, Department of Earth and Planetary Sciences	n/a	1.53	mgs: 95.8 dol: 3.7	2.78	2.87	3.01	8

Minerals	Source	Location	Ideal formula	Sample thickness (mm)	Orientations measured	Sample color	Density (g cm⁻³)
Calcite spar	Departmental collection, Washington University, Department of Earth and Planetary Sciences	N/A	$CaCO_3$	aa: 1.56 ac: 1.35	aa, ac	Colorless	2.72
Calcite hex	Departmental collection, Washington University, Department of Earth and Planetary Sciences	N/A	$CaCO_3$	aa: 0.975 ac: 0.920	aa, ac	Colorless	2.72
White dolomite	Excalibur Mineral Corp., Charlottesville, Virginia	Eugul, Navarre, Spain	$CaMg(CO_3)_2$	aa: 0.956 ac: 1.29	aa, ac	White	2.86
Grey dolomite	Excalibur Mineral Corp., Charlottesville, Virginia	Eugul, Navarre, Spain	$CaMg(CO_3)_2$	aa: 1.35 ac: 1.04	aa, ac	Light grey	2.86
Magnesite	Excalibur Mineral Corp., Charlottesville, Virginia	Brumado, Bahia, Brazil	$MgCO_3$	1.53	Intermediate	Colorless	2.98
Rhodochrosite	Excalibur Mineral Corp., Charlottesville, Virginia	Wudong Mine, Wushuo Prefecture, Guangxi Zhuang, China	$MnCO_3$	1.64	Intermediate	Pink	3.7

Note: Porosities for all orientations of samples 33-1 and 17-4 and Carrara Marble were calculated using skeletal density of the bulk powdered sample. For rocks, "II" indicates heat flow parallel to foliation plane, and "IL" indicates heat flow perpendicular to foliation. For minerals, "*aa*" indicates heat flow parallel to the *c*-axis, and "*ac*" indicates heat flow perpendicular to the *c*-axis. Mineral proportions are determined by X-ray diffraction (see Experimental Methods in text), and mineral abbreviations are as follows: cc—calcite; qtz—quartz; dol—dolomite; kfs—potassium feldspar; chl—chlorite; for—forsterite; mgs—magnesite. Other abbreviations: LFA—laser flash analysis; EJB—Eureka Valley–Joshua Flat–Beer Creek aureole; hex–hexagonal calcite sample; N/A—not available.

out connected pore space. (3) A Quantachrome multipycnometer was used to measure the bulk density of samples that were powered to <150 µm to allow helium to penetrate previously unconnected pore space. Sample powder was weighed in a sample chamber, which was then placed in a sealed chamber in the multipycnometer. Helium was added to a reference chamber to a measured pressure of ~117 kPa and opened to the sample chamber. With helium present in both the reference and sample chamber, the new pressure was recorded, and the ratio of reference to sample plus reference chamber pressure was used to calculate the volume of the sample.

These three measurements were combined to calculate total porosity and connected porosity after Avard and Whittington (2012).

Isobaric Heat Capacity

The heat capacity of powdered rock samples was measured using a Perkin-Elmer DSC 8500 differential scanning calorimeter (DSC). Powdering was necessary to ensure uniformity given the small capacity of sample pans in the DSC (25–50 mg). All experiments were performed using gold sample pans and a sapphire reference standard. Our heat capacity measurements of single-crystal calcite varied <2% from literature values across the temperature range ~275–900 K (Jacobs et al., 1981). Heat capacity was measured at discrete intervals of 25 K across a range of temperatures from ~275 to ~600 K (limestones) or to ~900 K (marbles). Experimental heat capacity results were fitted to the equation (Robie and Hemingway, 1995):

$$C_P = a + bT + cT^{-2}, \qquad (2)$$

where C_P is in J kg^{-1} K^{-1}, T is in Kelvin, and a, b, and c are experimental fitting parameters.

For minerals, we used published C_P data (calcite: Jacobs et al., 1981; dolomite: Krupka et al., 1985; magnesite: Robie and Hemingway, 1994; rhodochrosite: Moore, 1943). We combined these data for minerals with the modal mineralogy from XRD results to calculate ideal heat capacity for the rock samples to compare experimental results for powdered rock.

Thermal Diffusivity

We used a NETZSCH LFA 427, described by Bräuer et al. (1992), to measure thermal diffusivity. For a general descriptions of this method, which is commonly used in industry and materials science, see Maglić and Taylor (1992), Vozár and Hohenauer (2003, 2005), and Criss and Hofmeister (2017). For procedural details regarding our laboratory, see Pertermann and Hofmeister (2006).

In brief, samples were prepared as nearly circular disks between 0.75 and 2 mm thick, with a diameter of ~10 mm. All rock samples had grain sizes smaller than disk thickness, ensuring that measured D reflects the bulk mate-

rial rather than individual crystals. Samples were coated with one to two layers of graphite to aid in absorption of the laser pulse and emission of heat from the top side of the sample.

The method is contact free: A Nd:GGG laser is used to heat the bottom of the sample. As heat diffuses through the sample, an IR detector on the opposite side of the sample from the laser records the change in emissions with time, which is directly related to the change in temperature. Thermal diffusivity of the sample at the given temperature is obtained by fitting the time-temperature (t-T) acquisitions using the model of Cowan (1963) at ambient temperature and Mehling et al. (1998) above ~300 K to remove spurious effects of ballistic radiative transfer.

Maximum temperatures attained depended upon the sample maintaining physical integrity at elevated temperature without the presence of confining pressure. For each sample, D is measured at discrete temperatures along a pre-programmed path. Each reported measurement is the average from t-T curves of between two and six laser shots at that temperature, to ensure reproducibility. Measurement uncertainty is highest near room temperature (up to 5%), decreasing to ~2% at elevated temperatures, as ascertained by comparison with steel, iron, graphite, and Pyroceram standards reference materials from the National Institute of Standards and Technology and the manufacturer (Henderson et al., 1998a, 1998b). These standards are opaque and also soft, so they do not transmit light ballistically and adhere well to thermocouples, permitting calibration against results obtained from conventional methods, e.g., that of Hust and Lankford (1984). Temperatures were calibrated against the well-established Curie points of iron and cobalt.

Sample Descriptions

Minerals

Calcite spar is colorless and transparent, and microprobe analysis (Table 2) indicates a nearly pure calcite crystal with trace quantities (<0.1 wt%) of magnesium, iron, and sodium. *Calcite hex* is a colorless, hexagonal calcite crystal (microprobe data unavailable).

The dolomite samples (*white dolomite*, *grey dolomite*) were cut from the same crystal. Both white and grey samples are nearly pure (Table 2) with small amounts of iron (FeO = 0.18–0.42 wt%) and manganese (MnO = 0.1 wt%), but total CaO + MgO is low relative to ideal dolomite. Trace impurities (<0.1 wt% oxide) include Al, Na, and Ti. The color of grey dolomite likely results from a larger proportion of FeO compared to white dolomite.

The translucent *magnesite* crystal includes substitutions of Mn, Fe, and Ca for magnesium, with Mg composing 98% of cation mass within the crystal (Table 2). Additional trace elements include Na, Al, and K.

The *rhodochrosite* sample is pink in hand specimen. Microprobe analysis (Table 2) indicates 1.4 wt% FeO, with a smaller amount of Mg and trace

TABLE 2. MINERAL CHEMICAL ANALYSIS (ELECTRON MICROPROBE ANALYSIS)

Sample	SiO$_2$	Al$_2$O$_3$	FeO	MnO	MgO	CaO	Na$_2$O	K$_2$O	SO$_3$	TiO$_2$	Cr$_2$O$_3$	CO$_2$	Total
Minerals													
Calcite spar	—	—	0.01	<0.01	0.02	56.51	0.01	0.01	—	<0.01	—	43.27	99.84
White dolomite	—	0.01	0.18	0.13	20.98	29.91	—	<0.01	—	<0.01	<0.01	47.29	98.50
Grey dolomite	—	<0.01	0.42	0.10	20.98	29.84	<0.01	—	—	<0.01	—	47.24	98.59
Magnesite	—	<0.01	0.31	0.35	45.40	0.22	0.03	—	0.01	n/a	n/a	52.13	98.45
Rhodochrosite	—	<0.01	1.36	58.92	0.29	0.04	0.02	<0.01	—	n/a	n/a	37.85	98.49
Minerals in rocks													
33-1, forsterite	43.11	—	0.64	0.04	57.53	0.04	—	<0.01	n/a	0.01	—	n/a	101.36
33-1, dolomite	—	—	0.08	0.01	21.24	30.80	0.01	0.01	n/a	0.01	—	n/a	99.23
33-1, clinochlore	30.36	20.03	0.21	—	34.60	0.11	—	0.02	n/a	0.07	0.01	n/a	100.42
33-1, calcite	—	—	—	0.01	1.78	53.94	<0.01	<0.01	n/a	<0.01	<0.01	43.69	99.43
Threshold marble	—	—	<0.01	0.00	0.21	57.10	—	<0.01	n/a	0.01	<0.01	43.64	100.96
Black marble	—	0.01	0.03	0.02	0.27	56.29	0.01	<0.01	n/a	0.01	<0.01	43.80	100.44
17-4, grey dolomite	—	—	0.03	0.01	21.08	31.04	<0.01	<0.01	n/a	<0.01	<0.01	47.07	99.23
17-4, white dolomite	—	0.01	0.03	0.02	20.99	30.73	<0.01	<0.01	n/a	0.01	0.01	47.16	98.94
Carrara Marble	—	<0.01	0.01	—	0.46	59.05	—	—	n/a	—	—	42.68	102.20
AW-05, dolomite	—	0.16	0.38	0.03	21.32	31.83	<0.01	<0.01	—	—	—	47.11	100.83
AW-05, calcite	—	0.00	0.05	0.01	1.13	58.14	—	<0.01	—	—	—	43.32	102.65
Mgs conglomerate, magnesite	0.13	0.06	—	0.01	42.80	2.74	0.06	0.02	0.10	n/a	n/a	52.05	97.96
Mgs conglomerate, dolomite	—	0.03	<0.01	<0.01	25.55	24.92	0.02	<0.01	0.02	n/a	n/a	48.50	99.04

Note: All results are in weight percent. Results for most samples are the average of two or more point analyses. "n/a" indicates oxide not in search parameters. Dashes indicate oxide note detected. <0.01 indicates value detected was within calculated analytical error. Totals above 100% may result from CO$_2$ loss due to beam damage, which increases residual cation concentration, or from buried higher atomic-number phases. Cation detection limit varied between ~0.004 and 0.012 wt%. Data are unavailable for limestone samples. See Table S1 (text footnote 1) for measurement standards and analytical error. Mgs—magnesite.

quantities of Al, Ca, Na, and K. A solid solution exists between pure rhodochrosite and siderite (FeCO$_3$), and the mineral formula of this specimen is (Mn$_{0.97}$Fe$_{0.02}$Mg$_{0.005}$)CO$_3$.

Sedimentary Rocks

Sample *TF-001* is a fossiliferous limestone composed primarily of calcite with ~3 wt% quartz (Table 1). The sample has a wide range of grain sizes, with the largest grains concentrated in the center of the matrix between fossils (Fig. 3A). Fine-grained material composed mostly of calcite with minor quartz occurs in the center of fossils and along the boundaries between clusters of smaller fossils. Pore space is estimated at 9%, which is the difference between the measured density and the density calculated as the weighted average of the constituent minerals. Bulk rock chemical analysis shows small amounts of Si as well as Fe and Mg (Table 3).

Sample *TF-002* is a limestone dominated by ooids and rounded fossils. Ooids are fairly uniform in size, ranging from ~0.25 to 0.5 mm in diameter, and are composed of fine-grained bands radiating from a central point. Larger grains are concentrated in the matrix (Fig. 3B). This sample has the lowest amount of calcite of the four limestones (93.8 wt%) and the highest

φ (13%). Chemical analysis suggests that either XRD analysis overestimates quartz content by several percent (Table 3) or some heterogeneity exists within the sample, and also indicates that the sample has small amounts of Fe, Al, and Mg.

Sample *MO-05* (boundstone) is nearly pure calcite (Table 1) with small amounts of dolomite and quartz in a highly variable matrix, which lacks immediately recognizable fossils (Fig. 3C). Porosity (6%) is low compared to that of the above limestones, and not apparent in thin section. Bulk rock chemistry confirms a calcite-dominated mineralogy with small amounts of silica and magnesium (Table 3).

Sample *MO-07* (micrite) is nearly 100% calcite (Table 1), with a very small average grain size (~0.005 mm) and very low φ (~2%). Most of the sample is composed of indistinguishable small grains; however, clusters of larger grains of calcite occur randomly throughout (Fig. 3D). Chemical analysis confirms the nearly pure calcite makeup of this sample (Table 3).

Sample *KS-002* (dolomite rock) is largely dolomite (79%), but also contains ~11% potassium feldspar and 10% quartz (Table 1). Bulk chemical analysis shows that a small amount of Fe is present, but only trace quantities of Na, suggesting that feldspar is dominated by K. This sample is also typified by a high φ (15%), with an overall fine-grained matrix broken by larger detrital quartz and feldspar grains (Fig. 3E).
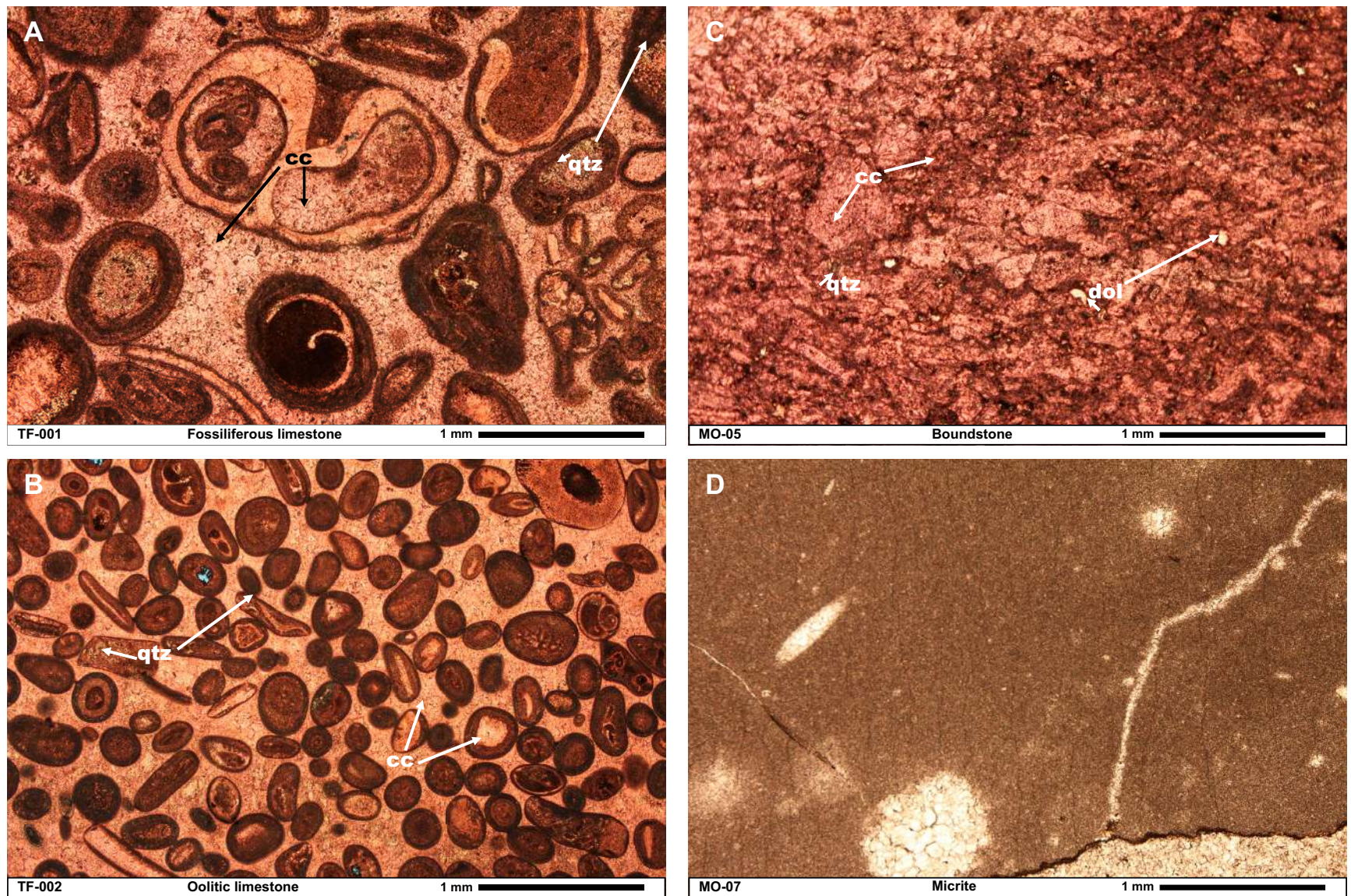
Figure 3 (*on this and following two pages*). Photomicrographs of rock samples (Table 1) in plane-polarized light. See text for sample descriptions. Samples TF-001, TF-002, MO-05, KS-002, 33-1, and 17-4 were treated with alizarin to highlight calcite where present (red tint). All images are at the same scale. Polymineralic samples have example phases marked according to mineralogy: qtz—quartz; cc—calcite; dol—dolomite; for—forsterite; kfs—potassium feldspar; chl—chlorite. (A) Sample TF-001, fossiliferous limestone, with minor qtz in ooids and some fossils. (B) Sample TF-002, oolitic limestone, with minor qtz in ooids and fossils; large pore space (pale blue) in two upper left ooids is likely a result of sample preparation. (C) Sample MO-05, boundstone. (D) Sample MO-07, micrite, consisting of nearly pure cc; rare qtz is not visible at this scale.
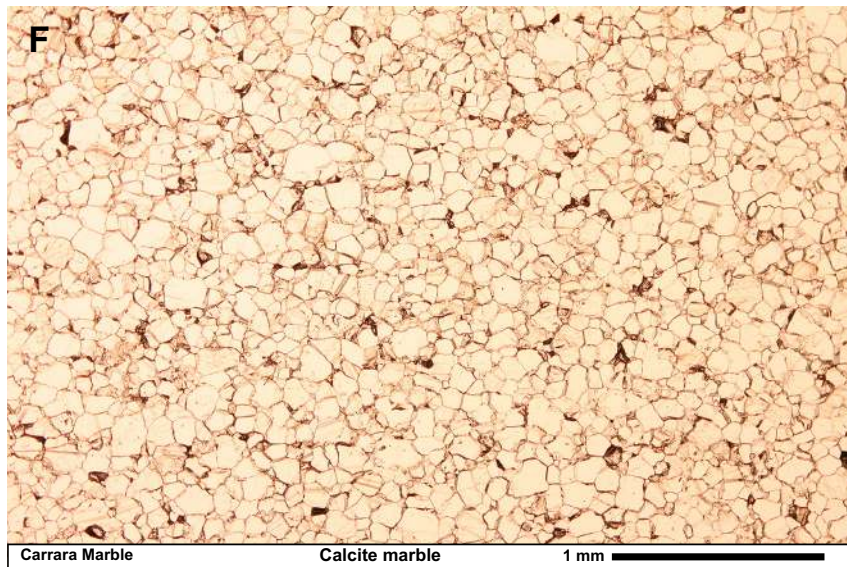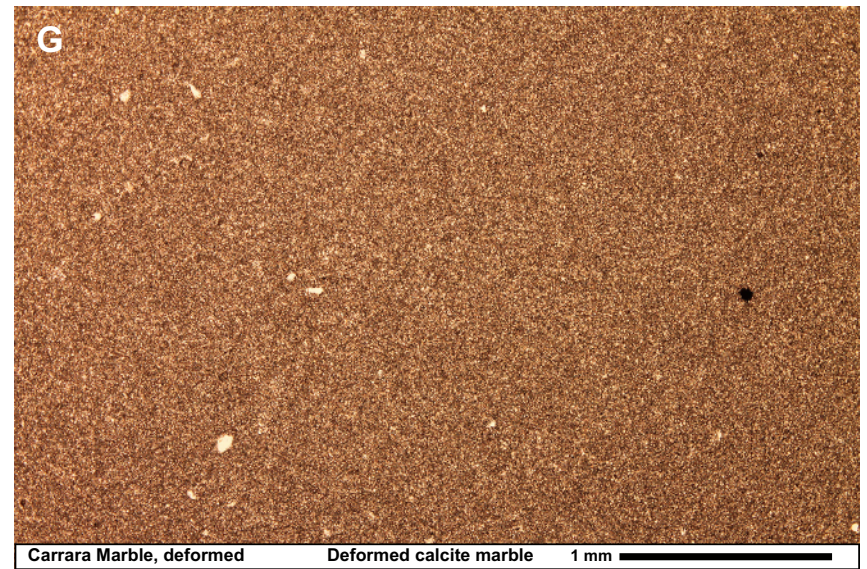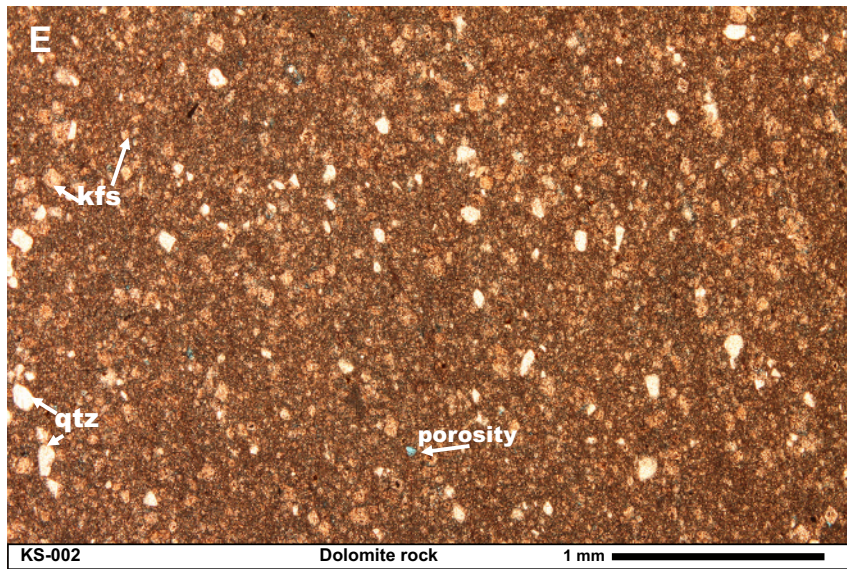
Figure 3 (*continued*). (E) Sample KS-002, dolomite rock; matrix is cc, and larger grains are qtz or kfs; porosity is visible as pale blue. (F) Carrara Marble; pure calcite. (G) Carrara Marble, experimentally deformed; pure calcite. (H) Threshold marble; pure calcite marble; note larger average grain size than Carrara Marble (F).
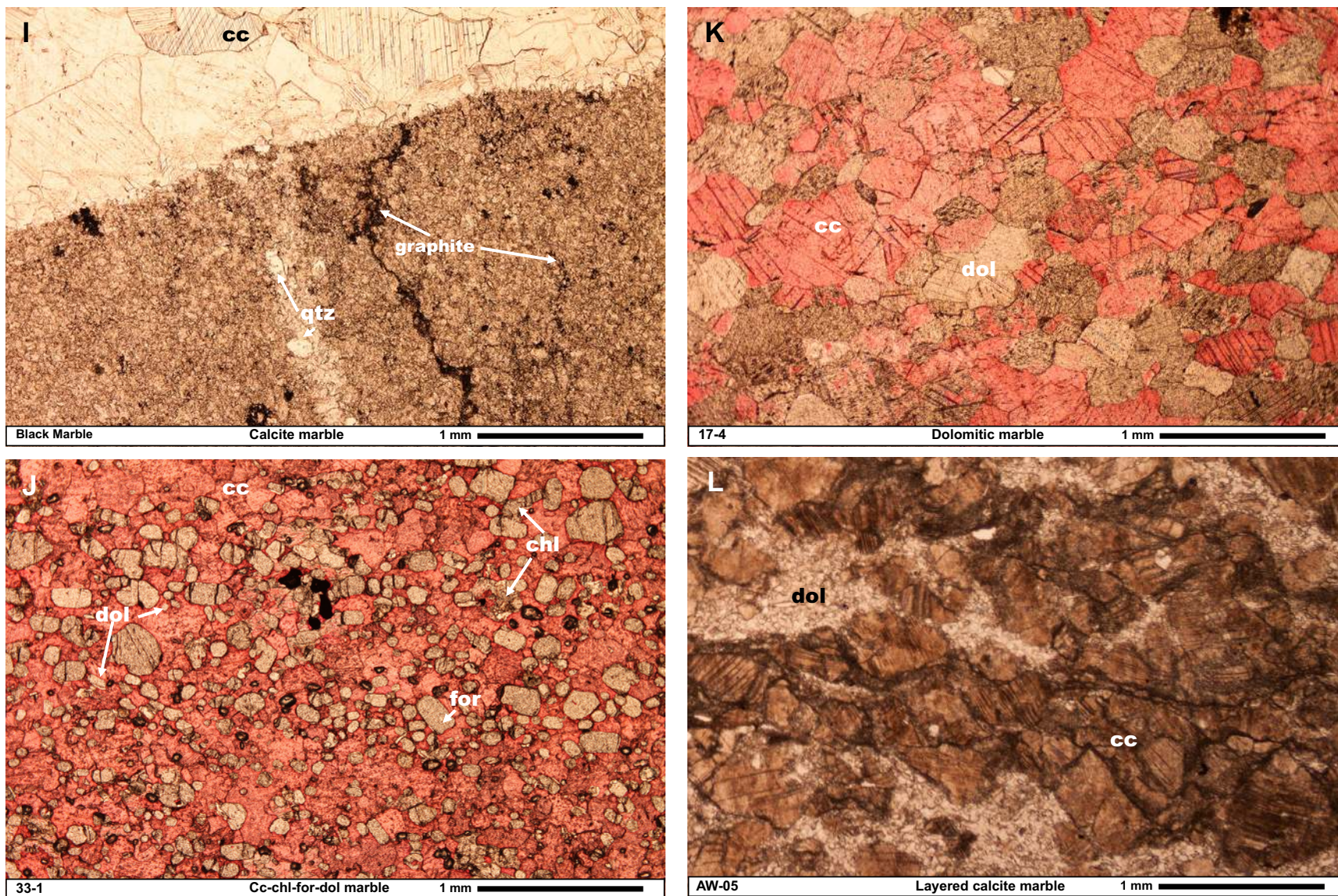
Figure 3 (*continued*). (I) Black marble; calcite marble with minor (0.9 wt%) qtz; black veins and spots may be graphite. (J) Sample 33-1, cc-chl-for-dol marble; cc is stained red; for appears as high-relief translucent grains, dol as lower-relief translucent grains; chl is visible as alteration between grains. (K) Sample 17-4, dolomitic marble; abundant cc (red) and dol (translucent) compared to X-ray diffraction results (Table 1; ~94% dol versus ~6% cc) suggests mineralogical heterogeneity in the sample (see text for discussion). (L) Sample AW-05, layered cc marble; matrix is fine-grained dol; chl is visible as alteration along cc grains (brown); sample layering and textural variation are not visible at this scale.

TABLE 3. MAJOR-ELEMENT CHEMICAL ANALYSIS OF ROCK SAMPLES

Sample	Total carbon	Graphitic carbon	SiO₂	Al₂O₃	Fe₂O₃ (total Fe)	MnO	MgO	CaO	Na₂O	K₂O	TiO₂	P₂O₅	LOI	Total
Detection limit (%)	0.01	0.05	0.01	0.01	0.01	0.00	0.01	0.01	0.01	0.01	0.01	0.01	0.01	
TF-001	n/a	n/a	2.72	0.09	0.74	0.06	0.44	53.38	0.02	0.03	<0.01	0.08	41.66	99.22
TF-002	n/a	n/a	3.01	0.22	0.37	0.05	0.38	52.73	0.05	0.10	0.01	0.13	41.17	98.20
MO-05	n/a	n/a	0.41	0.08	0.19	0.04	0.17	55.75	0.01	0.03	<0.01	0.02	42.41	99.10
MO-07	11.70	0.10	0.49	0.16	0.05	0.01	0.22	55.28	0.01	0.04	0.01	<0.01	43.42	99.70
KS-002	n/a	n/a	14.19	1.50	0.54	0.02	17.85	25.52	0.03	1.02	0.05	0.03	39.28	100.00
Black marble	11.70	0.06	1.30	0.09	0.10	0.02	0.29	54.56	0.02	<0.01	0.01	0.04	43.22	99.64
33-1	7.71	0.05	15.14	0.67	0.39	0.03	22.87	32.47	<0.01	<0.01	0.04	0.03	28.56	100.20
17-4	12.40	0.08	0.67	0.02	0.07	0.01	21.50	30.45	0.01	<0.01	<0.01	0.02	46.21	98.97
AW-05	11.00	n/a	4.63	1.58	0.54	0.02	11.4	40.17	0.03	0.06	0.06	0.03	39.99	98.51

Note: See Experimental Methods in text for description of analytical methods, standards, and analytical uncertainty (Table S1 [text footnote 1]). Total does not include total carbon or graphitic carbon. n/a—analysis was not performed for the sample. All values are in mass percent. LOI—loss on ignition.

Metamorphic Rocks

White *Carrara Marble* from Tuscany, Italy, has been quarried since the time of the Roman Empire. XRD revealed calcite as the only mineral phase, and microprobe analysis shows small amounts of Mg and only trace amounts of Fe and Al (Table 2). Two different samples of Carrara were used in this study: a fresh sample and an experimentally deformed sample. The fresh sample shows mostly interlocking grains of calcite with occasional fine-grained interfaces between larger grains (Fig. 3F). In hand specimen, the outer layers of the fresh sample are brittle, but the interior remains relatively coherent. A sample deformed at room temperature by George Dresden was provided by Brian Evans (Xu and Evans, 2010), with deformation resulting in an order-of-magnitude decrease in average grain size (Table 1; Fig. 3G), as well as a fourfold increase in φ (4% fresh, 16% deformed).

Threshold marble is a commercial tile. This sample is also a pure calcite marble with ~4% porosity, but has a slightly larger average grain size than Carrara Marble (0.08 mm versus 0.06 mm). Threshold marble contains calcite crystals with strong twinning and cleaner grain boundaries than Carrara (Fig. 3H). Microprobe analysis indicates calcite crystals with minor Mg substitution (Table 1).

Black marble is 99% calcite, containing ~1% of grey quartz veins. Like Carrara Mable and Threshold marble, Black marble contains small amounts of magnesium (Table 3) but lower amounts of total CaO (Table 3), and some quartz (Table 1) which the others lack. In thin section, this sample has what appears to be cloudy veins of graphite (Fig. 3I), but chemical analysis by combustion revealed only small amounts (0.06 wt%). In addition to quartz and (possibly) graphite veins, bands of large, interlocking calcite crystals crisscross the sample (Fig. 3I). Porosity of this marble is relatively low (4%).

Sample *33-1* is a calcitic marble (calcite = 58.5%) with high contents of dolomite (10.3%), forsteritic olivine (16.0%), and chlorite (15.2%) as indicated by XRD (Table 1). In hand specimen, the sample has alternating white and grey layers of thicknesses between 0.5 and 2 cm which are not apparent in thin section (Fig. 3J),

but may result from variable amounts of olivine or chlorite. Both olivine and chlorite are nearly pure Mg end members (Table 2). Dolomite crystals are modestly deficient in Mg, whereas calcite contains up to 1.8 wt% MgO. Bulk rock chemical analysis (Table 3) suggests there is insufficient alumina present to support the 15 wt% chlorite indicated by XRD. This may be a scale effect due to compositional heterogeneity between white and grey layers. In thin section (Fig. 3J), large grains of calcite surround rounded to subrounded grains of olivine and dolomite, and no porosity is evident, which is confirmed by density measurements (Table 1). Average grain size is larger than that of all other rock samples except 17-4.

Sample *17-4* is a dolomite-dominated marble from the same metamorphic aureole as sample 33-1, and contains ~6% calcite. Like 33-1, this sample has white and grey layers in hand specimen, which may result from variable proportions of calcite and dolomite (Fig. 3K). The composition of dolomite is homogeneous throughout (Table 2). Bulk rock chemical analysis found <1% of silica that was not detected by the XRD. 17-4 has the largest grain size of any of our samples (0.4 mm), but no measurable φ (Table 1).

Sample *AW-05* is a foliated and lineated calcitic marble (calcite = 56%) accompanied by a substantial proportion of dolomite (~37%) and some chlorite (~7%) (Table 1). Like for the other marbles, microprobe analysis indicated that dolomite in this sample is somewhat deficient in Mg. The hand specimen is white with thin foliation planes (1–2 mm). In thin section (Fig. 3L), large calcite crystals form foliation planes of moderately sized interlocking grains surrounded by microcrystalline dolomite. Dolomite grains are highly altered near large calcite crystals, but fresh where large calcite crystals are absent. Average grain size of dolomite matrix is ~0.1 mm, whereas calcite crystals are as large as 2.0 mm. The bimodal distribution of grain sizes results in an average grain size of ~0.7 mm. Porosity is minimal (<1%).

The *magnesite conglomerate* sample is largely magnesite with a small amount of accessory dolomite and ~8% porosity (Table 1). The magnesite is deficient in Mg and contains large amounts of Ca, with smaller amounts of Si, Al, Na, and K; the dolomite has excess Mg and is deficient in Ca (Table 2).

■ RESULTS

Heat Capacity

Experimental C_P results on the rocks studied here agree reasonably well with C_P calculated using literature data on mineral components and modal mineral proportions from XRD analysis (Fig. 4). Measurements of sedimentary samples were limited to <~600 K. Metamorphic carbonate rocks heated to higher T depart significantly from calculated C_P. Powders for samples heated to high T showed signs of significant alteration: typically, the powder darkened, and mass of the sample dropped by 1%–2%, consistent with the onset of decarbonation reactions. Thus, fits of experimental C_P to Equation 2 (Table 4A) do not include measurements above 600 K.
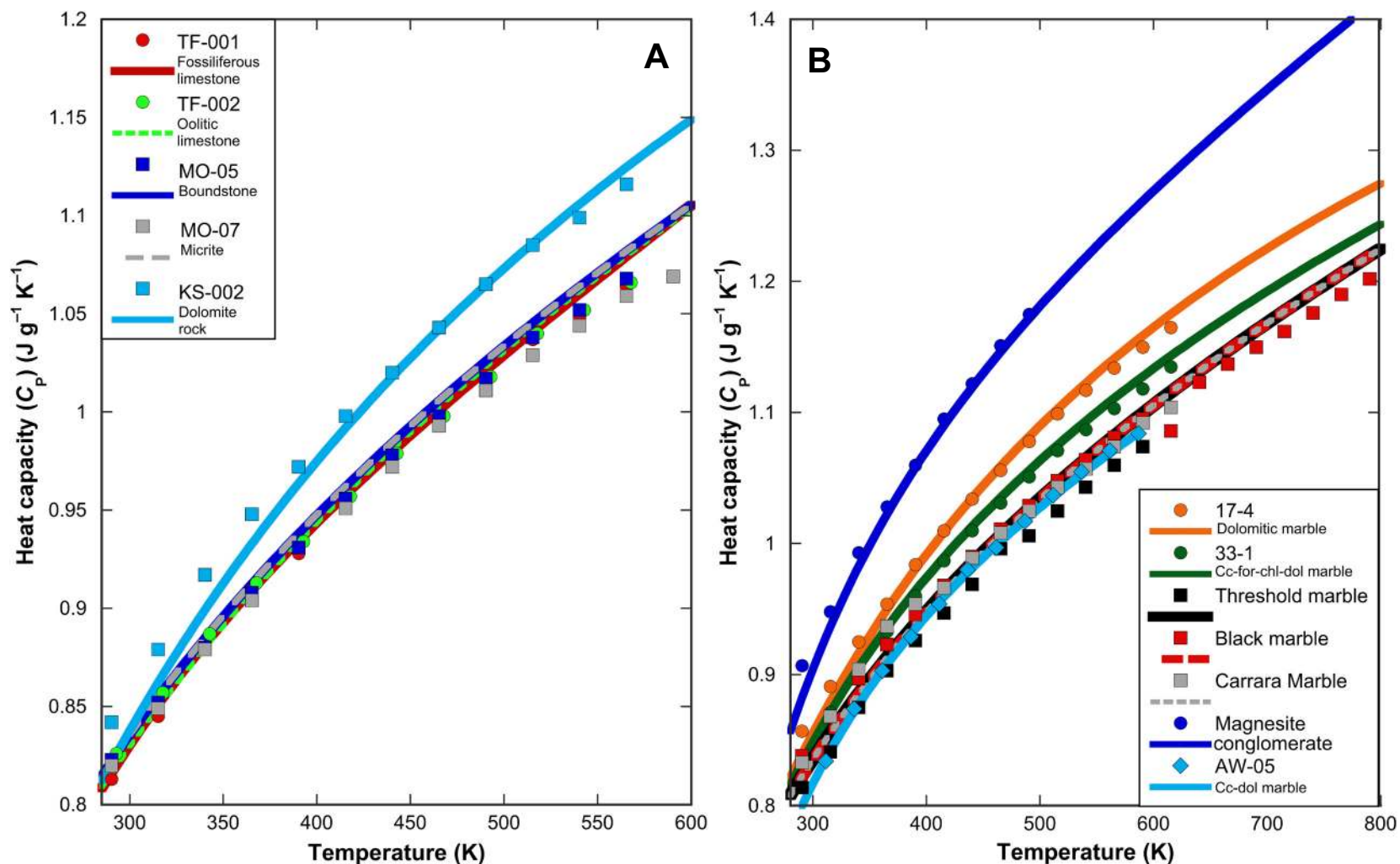
Figure 4. Isobaric heat capacity (C_P) of limestone (A) and marble (B) samples. Lines show C_P calculated from modal mineralogy (Table 1) after Robie and Hemingway (1995). Filled symbols are direct measurements of C_P using powdered rock samples.

TABLE 4A. HEAT CAPACITY FITTING PARAMETERS

Sample	a	b	c (× 10⁶)	R^2	Measured temperature range (K)
TF-001	776.98	0.574	−10.80	0.9995	265–565
TF-002	760.16	0.598	−8.82	0.9996	268–568
MO-05	735.24	0.641	−8.16	0.9996	265–565
MO-07	780.60	0.548	−9.89	0.9994	265–665
KS-002	833.60	0.578	−13.10	0.9996	265–565
Carrara Marble	846.54	0.470	−12.14	0.9991	265–615
Threshold marble	767.66	0.567	−9.60	0.9989	265–615
Black marble	828.97	0.499	−11.29	0.9995	265–790
17-4	839.40	0.587	−12.71	0.9993	265–615
33-1	850.60	0.522	−13.85	0.9994	265–765
AW-05	850.24	0.476	−15.47	0.9997	261–661
Magnesite conglomerate	800.55	0.870	−12.12	0.9998	265–515
Calcite	828.22	0.517	−13.11	0.9994	285–870
Dolomite	955.42	0.449	−21.43	0.9996	285–870
Magnesite	962.12	0.620	−21.73	1.0000	298–1000
Rhodochrosite	669.87	0.496	−10.27	0.9999	298–600

Note: Fitting parameters for Equation 2 (see text). Mineral data are from the literature (see Experimental Methods in text for references).

TABLE 4B. THERMAL DIFFUSIVITY FITTING PARAMETERS

Sample	e	f	g (× 10⁻⁴)	R^2	Measured temperature range (K)
TF-002	10,123	1.625	1.62	0.998	293–478
MO-05	11,746	1.599	−1.26	0.998	295–529
MO-07	10,861	1.573	0.37	0.997	296–531
KS-002	10,773	1.564	1.37	0.994	293–597
Carrara Marble (run 1)	472	1.118	0.29	1.000	294–702
Carrara Marble ("trapezoid" run)	574	1.083	−4.36	0.993	297–599
Carrara Marble (deformed)	9392	1.602	1.28	0.999	294–870
Threshold marble	3188	1.370	0.72	0.997	295–877
Black marble	15,382	1.638	0.64	0.995	294–880
17-4, grey dolomite, parallel	6150	1.363	—	1.000	299–964
17-4, grey dolomite, perpendicular	5813	1.373	—	0.999	297–1013
17-4, white dolomite, parallel	3051	1.287	—	1.000	300–1013
17-4, white dolomite, perpendicular	11,032	1.503	—	0.997	298–1013
33-1, white dolomite, parallel	1130	1.206	−0.11	0.997	294–774
33-1, white dolomite, perpendicular	5182	1.439	0.00	0.998	293–681
AW-05	3282	1.364	1.94	1.000	295–777
Magnesite conglomerate	4035	1.366	6.87	0.987	295–574
Calcite spar, *aa*	3708	1.360	1.30	1.000	296–888
Calcite spar, *ac*	4270	1.393	0.90	0.999	296–1008
Dolomite, grey, *aa*	6569	1.371	—	1.000	294–898
Dolomite, grey, *ac*	3278	1.264	—	1.000	297–766
Dolomite, white, *aa*	6770	1.380	—	0.990	295–483
Dolomite, white, *ac*	12,007	1.467	—	1.000	298–547
Magnesite	8525	1.334	—	0.999	296–615
Rhodochrosite	6023	1.396	—	0.998	296–634

Note: All samples were fit to Equation 3 (see text). *aa* and *ac* refer to heat flow parallel and perpendicular to the c-axis of the mineral, respectively. Parallel and perpendicular refer to sample cut such that heat flow is parallel or perpendicular to bedding.

TABLE 4C. THERMAL CONDUCTIVITY FITTING PARAMETERS

Sample	h	i (× 10⁻³)	j (× 10⁴)	n	R²	Measured temperature range (K)
TF-002	−18.14	9.41	−26.50	350.10	0.9998	293–565
MO-05	−17.59	9.91	−12.40	323.54	1.0000	295–529
MO-07	0.40	−1.75	5.90	42.57	1.0000	296–531
KS-002	−7.18	2.79	-8.30	176.52	0.9998	293–565
Carrara Marble (run 1)	−1.31	0.43	-0.99	53.64	0.9991	294–615
Carrara Marble ("trapezoid" run)	−3.32	1.15	2.19	87.93	0.9998	297–615
Carrara Marble (deformed)	0.40	−0.06	9.85	10.13	0.9989	294–615
Threshold marble	−8.55	2.96	−18.50	215.73	0.9995	295–615
Black marble	−17.11	7.10	−27.50	364.38	0.9978	294–790
17-4, average	−4.75	0.96	−4.34	177.74	1.0000	295–640
33-1, average	−3.84	1.22	−1.59	118.03	1.0000	295–615
AW-05	−11.71	5.32	−20.30	269.17	0.9997	295–587
Magnesite conglomerate	−13.49	8.10	−22.50	315.51	0.9990	295–515
Calcite spar, *aa*	−1.22	0.47	6.53	69.88	0.9990	296–870
Calcite spar, *ac*	2.28	−0.76	20.30	−11.93	0.9987	296–870
Dolomite, grey, *aa*	−11.96	3.87	−15.60	330.02	0.9999	294–870
Dolomite, grey, *ac*	−7.01	1.79	−10.40	234.94	0.9995	297–870
Dolomite, white, *aa*	−1.83	−1.26	1.32	143.56	1.0000	295–483
Dolomite, white, *ac*	−37.78	19.69	−46.60	759.75	1.0000	298–483
Magnesite	15.07	−10.45	41.60	−85.25	0.9996	296–634
Rhodochrosite	−6.92	2.12	−2.07	207.46	1.0000	296–600

Note: All samples were fit to Equation 4 (see text). *aa* and *ac* refer to heat flow parallel and perpendicular to the c-axis of the mineral, respectively. Parallel and perpendicular refer to sample cut such that heat flow is parallel or perpendicular to bedding. Results should not be extrapolated beyond the reported temperature range.

Because initial C_P measurements on rock samples TF-001, 17-4, and 33-1 and the magnesite conglomerate sample differed from calculated C_P by >3%, duplicate experiments were performed on these samples, and all were within 2% of calculated C_P. All final results were consistent to <2% at temperatures between 360 and 600 K. In the temperature range 280–360 K, all repeat experiments were within 3% of C_P calculated with literature data except that for the magnesite conglomerate, which differed by <4% in this temperature range. This may be due to adsorbed water on the powder used for measurement, as water has a heat capacity >4000 J kg⁻¹ K⁻¹ at room T (e.g., He et al., 2015). The powder for the second run (but not the first) was dried in an oven at ~400 K for 24 h. Variations of 1%–3% are reasonable given the experimental uncertainty and uncertainty in modal mineral proportions.

Thermal Diffusivity of Minerals

The thermal diffusivity of calcite spar was measured from ~300 to 900 K in two orientations: with heat flowing parallel to the *c*-axis (*aa*), and with heat flowing perpendicular to the *c*-axis (*ac*). At room temperature (296 K), D for calcite was very similar for both orientations: 1.66 mm² s⁻¹ for *aa* and 1.63 mm² s⁻¹ for *ac* (Fig. 5). D decreased rapidly on heating to ~500 K, then decreased more slowly at higher temperatures. For the *ac* orientation, D decreased more

rapidly and was ~3%–10% lower than for *aa*. By 888 K, D was ~0.47 mm² s⁻¹ for *aa* and ~0.43 mm² s⁻¹ (886 K) for *ac*.

Dolomite had consistently higher D than calcite, varying between 2.82 mm² s⁻¹ for white dolomite in the *ac* orientation at 298 K and 2.46 mm² s⁻¹ for grey dolomite (*ac*) at 297 K. As with calcite, D again decreased rapidly in the range 300–500 K, and more slowly above ~700 K. Thermal diffusivity reached ~0.74 mm² s⁻¹ at 766 K for grey dolomite in both orientations.

Magnesite and rhodochrosite form a solid solution, and given the lack of anisotropy in heat flow for calcite and low anisotropy in dolomite, an orientation between [001] and [100] was measured for both minerals. The Mg end-member magnesite had the highest D of any carbonate sample across the range of temperatures measured, decreasing from 4.36 mm² s⁻¹ at 296 K to 1.64 mm² s⁻¹ at 615 K. D for the Mn end-member rhodochrosite was between that of dolomite and that of calcite, decreasing from 2.16 mm² s⁻¹ at 296 K to 0.71 mm² s⁻¹ at 634 K.

Data for all thermal diffusivity results (Table 5) were fit to the equation (see Table 4B):

$$D(\text{mm}^2\ \text{s}^{-1}) = eT^{-f} + gT,\qquad(3)$$

where T is in Kelvin. The form of this equation was proposed by Hofmeister et al. (2014) to reproduce dD/dT for minerals with diverse structures and chem-

Figure 5. Thermal diffusivity (*D*) of minerals measured for this study. For minerals measured in multiple orientations, *aa* indicates heat flow parallel to the *c*-axis, and *ac* heat flow perpendicular to the *c*-axis (c = [100]) Note that "calcite hex" is a hexagonal-shaped sample of calcite. Crystal orientation has only a small influence on *D* at low temperature, and negligible influence at temperatures above ~500 K.
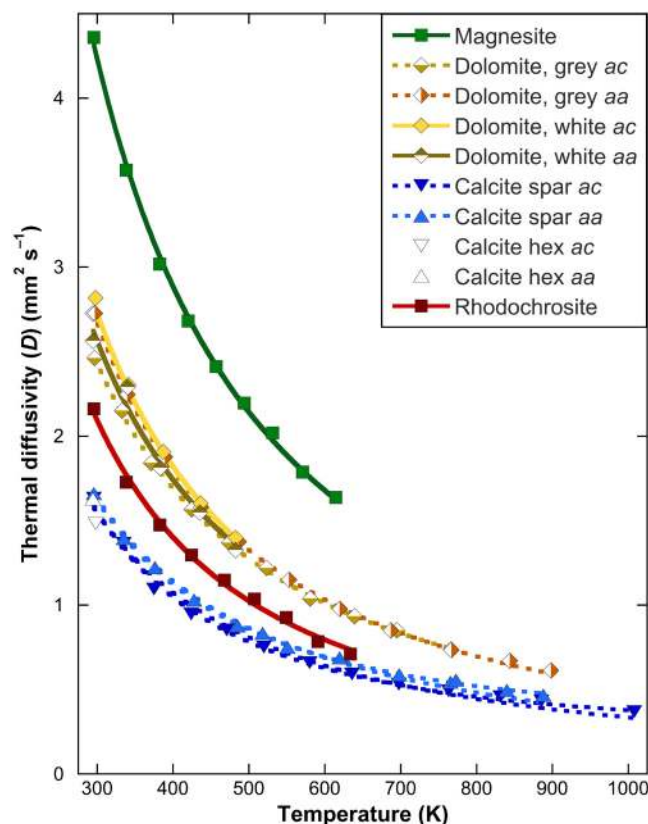
ical compositions, but applies to rocks as well (see the following sections). The terms *e* and *f* describe the reduction in *D* over the temperature range of ~300–600 K, and the *g* term corresponds to an increasing diffusive radiative contribution at higher temperatures. This form also fits various glasses, alkali halides, and semi-conductors, and some 200 species follow Equation 3. Hofmeister et al. (2014) argued that the form represents the sum of phonon scattering and diffusion of IR radiation (polaritons).

Thermal Diffusivity of Limestones

Dolomitic limestone KS-002 reflects the higher diffusivity of the mineral dolomite when compared to more calcitic limestones (Fig. 6). KS-002 has a *D* of 1.48 mm² s⁻¹ at 293 K, which decreases to 0.55 mm² s⁻¹ at 597 K. At similar temperatures, micrite MO-07 produced a *D* of 1.38 mm² s⁻¹ at 296 K, decreasing to 0.55 mm² s⁻¹ at 531 K. The samples with large fossil fragments or ooids produce the lowest *D* for limestones across the range of temperatures.

Boundstone MO-05 had a *D* of 1.30 mm² s⁻¹ at 295 K, decreasing rapidly to 0.48 mm² s⁻¹ at 529 K. Sample TF-001, a fossiliferous limestone, was only measured at 294 K, and produced a *D* of 1.04 mm² s⁻¹, similar to sample TF-002, an oolitic limestone with a *D* of 1.03 mm² s⁻¹ at 293 K. TF-002 was heated to 478 K, however, where *D* was 0.52 mm² s⁻¹.

Experimental data for limestones were fit to Equation 3 (Table 4B).

Thermal Diffusivity of Marbles

The thermal diffusivity of the marble samples varied more than that of the limestones, depending primarily on dolomite content (Fig. 7). Whereas room-temperature *D* for the AW-05, Black marble, and Threshold marble samples was comparable to that of limestone, at 1.45 mm² s⁻¹, 1.37 mm² s⁻¹, and 1.29 mm² s⁻¹, respectively, *D* dropped more rapidly on heating to 0.48 mm² s⁻¹ at 555 K for the Black marble and 0.60 mm² s⁻¹ at 561 K for the Threshold marble. Thermal diffusivity of sample AW-05, however, remained elevated at higher temperatures (0.73 mm² s⁻¹ at 523 K), where its *D* is similar to that of the dolomitic marbles. The marbles were measured to higher temperatures than the limestones, with *D* values approaching 0.3 mm² s⁻¹ for Black marble (0.31 mm² s⁻¹ at 880 K), calcite marble 33-1 (0.33 mm² s⁻¹ at 870 K), and Threshold marble (0.35 mm² s⁻¹ at 877 K). At room temperature (294 K), *D* for sample 33-1 was 1.49 mm² s⁻¹ perpendicular to layering and 1.24 mm² s⁻¹ parallel to layering, but this difference disappeared at high temperature. Dolomitic marble 17-4 had the greatest anisotropy at ambient temperature, from 2.00 mm² s⁻¹ (parallel, 300 K) to 2.01 mm² s⁻¹ (perpendicular, 298 K) for the white sample, and from 2.64 mm² s⁻¹ (parallel, 299 K) to 2.25 mm² s⁻¹ (perpendicular, 297 K) for the grey sample. These differences were reduced at higher temperatures.

The first disk of Carrara Marble had the lowest *D* of all samples measured at ambient temperature (0.82 mm² s⁻¹ at 294 K), falling to 0.33 mm² s⁻¹ at 702 K. The experimentally deformed sample had a higher *D* at room temperature (294 K), 1.10 mm² s⁻¹, but similar high-temperature values of 0.34 mm² s⁻¹ at 732 K and 0.29 mm² s⁻¹ at 870 K. A subsequent measurement of the same sample at room temperature (298 K) was only 0.53 mm² s⁻¹, suggesting that irreversible structural changes occurred in the sample during heating. As the sample is heated, grains within the disk expand differentially, opening new pore space, which remains upon cooling. The result is a more porous, friable sample whose intergrain thermal resistance is much higher.

Three additional disks of fresh Carrara were measured to assess reproducibility and explore the cause of low *D* in the first disk (Fig. 8, run 2, run 3, and trapezoid). Room-temperature *D* measurements were moderately higher at 0.91 mm² s⁻¹ (296 K), 0.94 mm² s⁻¹ (297 K), and 1.07 mm² s⁻¹ (297 K). In hand specimen, the sample was brittle to the touch, but when outer layers were removed, the interior was found to be less brittle. Disk 3 was reground twice, each time reducing outer-layer brittleness and increasing *D* at room *T* (Fig. 8). Finally, disk 4 (trapezoid) was measured at elevated temperature, and its *D* dropped rapidly to within error of results for disk 1 by ~500 K.

TABLE 5. THERMAL DIFFUSIVITY RESULTS

Temperature (K)	Thermal diffusivity ($mm^2\,s^{-1}$)	Temperature (K)	Thermal diffusivity ($mm^2\,s^{-1}$)	Temperature (K)	Thermal diffusivity ($mm^2\,s^{-1}$)	Temperature (K)	Thermal diffusivity ($mm^2\,s^{-1}$)	Temperature (K)	Thermal diffusivity ($mm^2\,s^{-1}$)
Calcite spar, *aa*		Calcite spar, *ac*		Calcite hex, *ac*		Grey dolomite, *aa*		Magnesite	
295.77	1.660	295.67	1.633	298.21	1.483	294.35	2.726	295.73	4.36
335.22	1.394	334.93	1.366	Calcite hex, *ac*		297.25	2.726	338.36	3.574
376.24	1.222	375.16	1.095	294.39	1.628	339.95	2.247	382.46	3.018
427.64	1.030	424.11	0.947	White dolomite, *aa*		389.55	1.877	420.05	2.682
485.40	0.876	470.72	0.853	294.79	2.563	437.15	1.580	457.11	2.411
518.00	0.833	519.86	0.752	340.11	2.291	486.75	1.375	493.97	2.195
551.00	0.750	580.07	0.659	383.19	1.811	553.05	1.151	531.35	2.019
619.72	0.687	635.78	0.591	435.57	1.548	619.85	0.978	570.93	1.787
698.14	0.588	697.75	0.533	482.76	1.326	687.15	0.850	614.61	1.638
765.69	0.543	763.35	0.493			767.15	0.732		
772.94	0.556	831.49	0.458			843.75	0.671		
839.90	0.495	885.62	0.433			898.35	0.613		
887.97	0.467	1007.6	0.368						
White dolomite, *ac*		Grey dolomite, *ac*		Rhodochrosite		TF-001		MO-05	
297.92	2.818	296.65	2.461	295.62	2.161	294.0	1.04	295.1	1.30
341.29	2.303	332.87	2.150	338.46	1.727	TF-002		334.5	1.04
387.4	1.907	371.35	1.840	382.77	1.474	293.5	1.03	377.9	0.82
436.25	1.602	424.9	1.566	424.56	1.297	335.3	0.87	429.7	0.65
482.66	1.398	474.14	1.369	467.82	1.148	376.9	0.74	479.2	0.54
547.47*	0.962*	523.29	1.219	507.3	1.037	426.6	0.61	528.7	0.48
		580.95	1.039	549.3	0.927	478.0	0.52		
		639.4	0.933	591.09	0.785				
		695.21	0.850	633.93	0.709				
		766.38	0.738						
MO-07		KS-002		Threshold marble		Black marble		AW-05	
296.2	1.38	292.9	1.48	295.2	1.29	294.0	1.37	295.4	1.45
333.4	1.16	346.0	1.18	337.4	1.12	338.5	1.16	334.9	1.25
377.4	0.96	397.6	0.97	378.9	0.99	379.4	1.00	377.3	1.09
429.8	0.79	448.4	0.80	431.1	0.85	425.1	0.82	428.6	0.93
480.8	0.66	497.0	0.71	493.5	0.72	489.6	0.59	476.4	0.81
531.3	0.55	547.5	0.61	561.3	0.60	555.2	0.48	523.1	0.73
		597.1	0.55	641.9	0.48	639.3	0.40	586.7	0.66
				716.2	0.42	720.8	0.36	643.5	0.60
				801.7	0.38	800.7	0.34	713.5	0.56
				877.5	0.35	879.8	0.31	776.8	0.53
Carrara Marble, run 1		Carrara Marble, "trapezoid" run		Carrara Marble, deformed		Magnesite conglomerate		17-4 white, parallel	
293.9	0.82	296.9	1.07	293.6	1.10	295.2	1.84	299.6	2.00
353.9	0.68	338.4	0.87	343.9	0.83	338.5	1.63	333.6	1.73
413.1	0.57	382.5	0.72	393.3	0.71	382.5	1.43	372.8	1.51
482.9	0.49	430.3	0.59	453.4	0.58	425.8	1.30	424.0	1.28
542.1	0.44	480.9	0.51	513.4	0.50	432.5	1.29	482.2	1.08
622.0	0.37	534.8	0.43	583.2	0.43	455.3	1.23	551.6	0.91
701.6	0.33	599.2	0.36	652.0	0.38	488.8	1.16	630.0	0.74
293.3	*0.84*	Carrara Marble, run 3		732.0	0.34	528.2	1.11	717.9	0.62
Carrara Marble, run 2		296.6	0.94	811.2	0.31	574.3	1.05	816.4	0.55
296.3	0.91	Carrara Marble, run 3, R1x		869.5	0.29	Carrara Marble, run 3, R2x		914.6	0.48
		296.7	1.14	*298.4*	*0.53**	296.7	1.15	1012.6	0.43

(*continued*)

Merriman et al. | Carbonate thermal diffusivity

TABLE 5. THERMAL DIFFUSIVITY RESULTS (*continued*)

Temperature (K)	Thermal diffusivity (mm² s⁻¹)	Temperature (K)	Thermal diffusivity (mm² s⁻¹)	Temperature (K)	Thermal diffusivity (mm² s⁻¹)	Temperature (K)	Thermal diffusivity (mm² s⁻¹)	Temperature (K)	Thermal diffusivity (mm² s⁻¹)
17-4 white, perpendicular		17-4 grey, parallel		17-4 grey, perpendicular		33-1, parallel		33-1, perpendicular	
298.2	2.01	298.8	2.64	297.4	2.25	294.3	1.24	294.5	1.49
334.8	1.80	335.1	2.23	336.2	1.95	335.4	1.04	384.8	0.96
372.7	1.57	372.5	1.93	373.9	1.73	390.4	0.85	484.8	0.68
422.6	1.27	422.4	1.62	422.7	1.47	484.3	0.63	676.5	0.43
482.3	1.06	481.8	1.35	482.1	1.24	614.7	0.48	870.0	0.33
551.2	0.83	551.3	1.14	551.5	1.03	745.5	0.40		
628.8	0.68	618.6	0.96	628.6	0.83	878.4	0.33		
717.4	0.51	699.4	0.79	718.1	0.67				
816.3	0.46	777.1	0.69	815.9	0.57				
914.5	0.41	865.5	0.62	915.0	0.50				
1012.6	0.35	964.3	0.55	1012.8	0.44				

Note: Italics indicate measurement post-heating. hex refers to the hexagonal shape of the sample. "R1x" and "R2x" indicate reground slices of Carrara Marble, run 3. See text for sample descriptions. *aa* and *ac* refer to heat flow parallel and perpendicular to the c-axis of the mineral, respectively. Parallel and perpendicular refer to sample cut such that heat flow is parallel or perpendicular to bedding.
   *Measurement not included in fitting (Table 4B).

Figure 6. Thermal diffusivity (*D*) of limestones and dolomite rock. Symbols are data collected, and lines are fits to data points. Given that most of these samples are dominated by calcite (except dolomite-dominated sample KS-002), the strongest control on bulk-rock *D* is likely textural. *D* generally decreases with increasing porosity (Table 1). Despite very high porosity (15%), dolomite rock KS-002 has higher *D* than all of the limestones measured. Note that "calcite" is a fit of the directionally averaged *D* of our calcite spar sample, as exact temperatures were not reproduced for each point for both orientations.
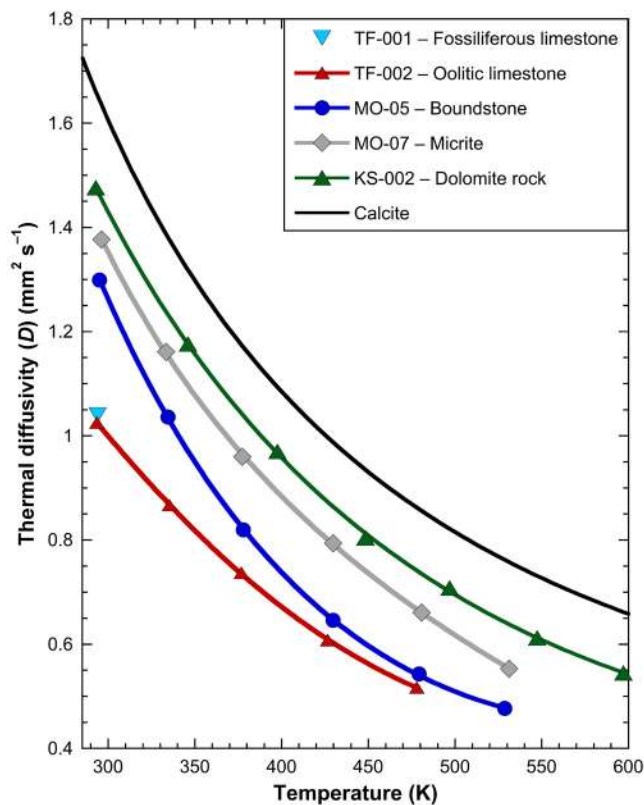
Experimental data for some of the Carrara runs (run 1, trapezoid, and deformed), Threshold marble, Black marble, sample 33-1, and magnesite conglomerate were fit to Equation 3. Data for sample 17-4 were fit to Equation 3.

Thermal Conductivity

For minerals, *k* was calculated using published values for ρ and C_P. Fitting parameters for C_P, *D*, and *k* can be found in Table 4. For rocks, *k* was calculated from Equation 1, with geometric ρ, and measured C_P which was fitted to Equation 2 to obtain values for the temperatures at which *D* was measured. For use in numerical modeling, the derived values of *k* (W m⁻¹ K⁻¹) were fitted to:

$$k = h + iT + jT^{-2} + nT^{-1/2}, \tag{4}$$

where *h*, *i*, *j*, and *n* are fitting parameters and *T* is in Kelvin. This empirical equation is commonly used to model heat capacity (e.g., Robie and Hemingway, 1995), and its success in fitting experimental data for thermal conductivity points to the strong influence of heat capacity in determining thermal conductivity (Equation 1). Propagation of errors using all three *measured* components of thermal conductivity results in a cumulative experimental uncertainty of 5.5% at ambient temperature, and 3% at elevated temperatures.

Mineral Thermal Conductivity

Because C_P and ρ typically vary less than *D* between carbonate minerals, mineral *k* mirrors *D*, with dolomite displaying high *k* at room *T*, and a steep negative *dk/dT* (Fig. 9). Room-temperature *k* was as high as
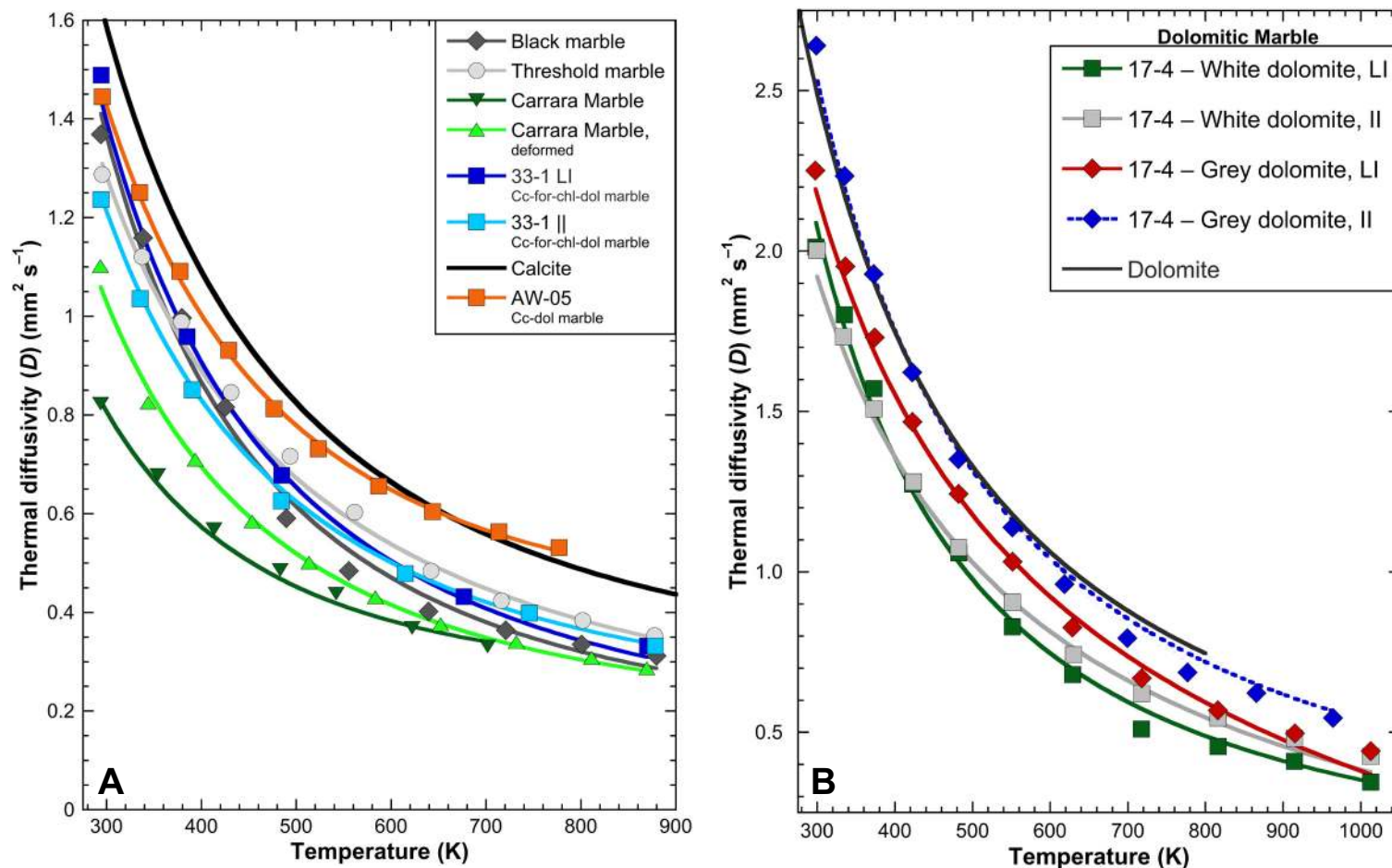
Figure 7. Thermal diffusivity (*D*) of marbles. Symbols are measured *D* data, and lines are fits to data points. The Carrara marble data shown here is run #1 (see Thermal Diffusivity of Marbles in the text for more information). (A) Calcite-dominated marble. The low *D* of Carrara Marble may be a consequence of poor cohesion of the outer layers of the sample (see text for discussion). Porosity was low for all samples, which resulted in a low spread of measured *D* for samples with similar mineralogy (Table 1). The lower *dD/dT* (*T* is temperature) for sample AW-05 may be a result of a high proportion of dolomite in the sample (37 wt%). cc—calcite; for—forsterite; chl—chlorite; dol—dolomite. (B) Dolomite-dominated marble (sample 17-4). "Dolomite" is directionally averaged dolomite (both white and grey dolomite). Directionally averaged calcite (calcite spar) is included for reference. For samples 33-1 (A) and 17-4 (B), "LI" indicates heat flowing perpendicular to (across) bedding, and "II" indicates heat flowing with bedding layers.

6.85 W m⁻¹ K⁻¹ (298 K) for grey dolomite (*ac* orientation) and as low as 5.97 W m⁻¹ K⁻¹ (297 K) for white dolomite (*ac* orientation). As with *D*, there is no strong dependence on orientation for either grey or white dolomite, as grey dolomite has a higher *k* at room *T* in the *aa* orientation, but white dolomite in the *aa* orientation has lower room-temperature *k* compared to the *ac* orientation. All *k* values for dolomite converge to a narrow range as temperature increases, and by ~500 K vary by <4%. The decrease in *k* as

temperature increases appears to level off and approach minimal values near ~2.3 W m⁻¹ K⁻¹ for the highest temperatures at which *D* was measured (898 K, grey dolomite [*aa*]).

Calcite shows a similar small dependence of *k* on orientation of the crystal, with nearly identical *k* at room *T*, departing slightly as temperature increases (Fig. 9). Calculated *k* for calcite remains roughly 60% that of any dolomite sample over the range of temperatures measured. For example, *k* at room *T*
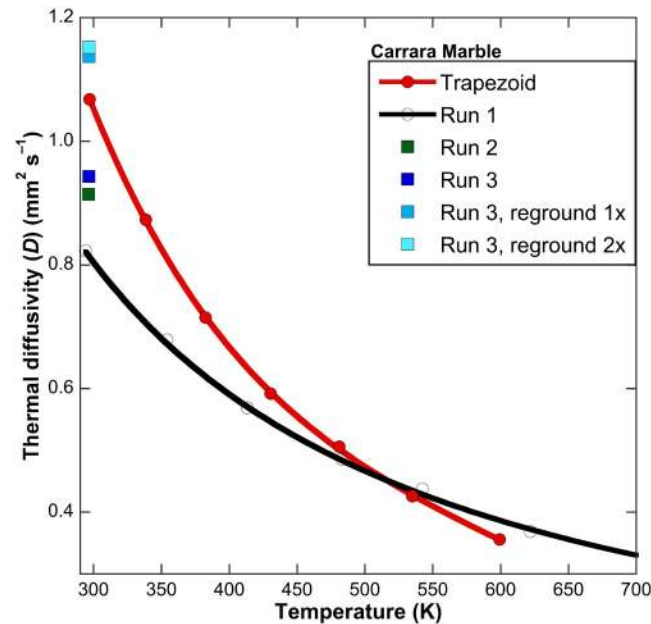
Figure 8. Effects on thermal diffusivity (*D*) of sample preparation on Carrara Marble. Runs 1–3 are disks of Carrara Marble (Table 1). "Trapezoid" is a trapezoidal cut of the same sample. "Run 3, reground" indicates the effects of grinding off outer layers of the run 3 disk to remove loosely coherent grains ("1×" is reground once, "2×" twice). Runs 2 and 3 were measured at room temperature only.

Figure 9. Thermal conductivity (*k*) and isobaric heat capacity (*C*ₚ) of carbonate minerals calculated using measured thermal diffusivity (*D*) and literature values for *C*ₚ and density (calcite—Jacobs et al. [1981]; dolomite—Krupka et al. [1985]; magnesite—Robie and Hemmingway [1994]; rhodochrosite—Moore [1943]). Solid lines are for *k*, dashed lines for *C*ₚ. For *C*ₚ, dark blue is magnesite, red is dolomite, black is calcite, and light blue is rhodochrosite. Line lengths are restricted by maximum measured *D*. For *k* measured in multiple orientations, *aa* indicates heat flow parallel to the *c*-axis, and *ac* heat flow perpendicular to the *c*-axis.

was ~3.7 W m^{-1} K^{-1} in the *aa* orientation, compared to ~6.6 W m^{-1} K^{-1} for grey dolomite (*aa*). At 620 K, this difference was ~2.1 W m^{-1} K^{-1} versus ~3.3 W m^{-1} K^{-1} respectively. Both minerals showed similar decreases in *k* over the range of temperatures in which *D* was measured. Calcite (*aa*) *k* drops by ~58% between 300 K and 890 K, and grey dolomite (*aa*) ~66% over the same temperature range.

For magnesite, the product of high *D* at all temperatures with higher ρ (3010 kg m^{-3}) and *C*ₚ (Fig. 9) combined to produce *k* ~80% higher than for dolomite. Although *D* of magnesite was measured to only 600 K, the *k* of magnesite was highly *T* dependent, dropping by 45% between 300 K and 600 K. Similar percentage decreases in *k* for both calcite and dolomite occurred across the same temperature range (~45%–48%).

The *k* of rhodochrosite was between that of calcite and dolomite. Lower *C*ₚ for rhodochrosite (~700 J kg^{-1} K^{-1} at 296K) is somewhat offset by higher ρ (3700 kg m^{-3}) resulting in a room-temperature *k* of 5.59 W m^{-1} K^{-1} (296 K), remaining higher than calcite and lower than dolomite to high *T* (2.50 W m^{-1} K^{-1} at 634 K). Rhodochrosite *k* shows a similar *dk/dT* to that of calcite and dolomite.

Limestone and Dolomite Rock Thermal Conductivity

As with most of the carbonate minerals, all samples of limestone and dolomite rock show a strong decrease in *k* with increasing *T* (Fig. 10A). Samples MO-07 (micrite) and KS-002 (dolomite rock) had very similar *k* values throughout the range of temperatures calculated, with MO-07 having a *k* of 3.14 W m^{-1} K^{-1} at 296 K, decreasing by ~50% to 1.64 W m^{-1} K^{-1} at 531 K and similar values for KS-002. Calcitic boundstone MO-05 had a higher *dk/dT* than any other sample calculated as *k* dropped by ~55% from an already low 2.74 W m^{-1} K^{-1} at 295 K to a very low 1.27 W m^{-1} K^{-1} at 529 K. Oolitic limestone TF-002 was similarly insulating at high *T*, but across the entire temperature range calculated (~2.0 W m^{-1} K^{-1} at 294 K, and ~1.2 W m^{-1} K^{-1} at 478 K).

Figure 10. Thermal conductivity (*k*) of carbonate limestone and marble samples, calculated using measured thermal diffusivity (*D*) and isobaric heat capacity (*C*$_P$) and measured geometric density. (A) Limestone *k*, including dolomite rock KS-002, calculated using measured *D* and *C*$_P$ and measured geometric density. Unlike for *D*, where KS-002 values were higher across the range of temperatures measured, samples KS-002 and MO-07 have similar *k* values at low temperature (*T*), with MO-07 having a higher *dD/dT*. This reflects the lower density of KS-002 resulting from high porosity, whereas MO-07 has very low porosity (Table 1). Calcite values are from directionally averaged calcite spar. (B) Marble *k* using measured *D* and *C*$_P$ with measured geometric density. Solid lines are rocks dominated by calcite; dashed lines, rocks dominated by dolomite; and the dotted line, magnesite. Values for dolomite, calcite, and samples 17-4 and 33-1 are directionally averaged. Carrara Marble data are from run 1 (Fig. 8). Low *dD/dT* for the magnesite conglomerate likely results from the higher *D* of magnesite relative to dolomite (see Fig. 5). cc—calcite; for—forsterite; chl—chlorite; dol—dolomite.
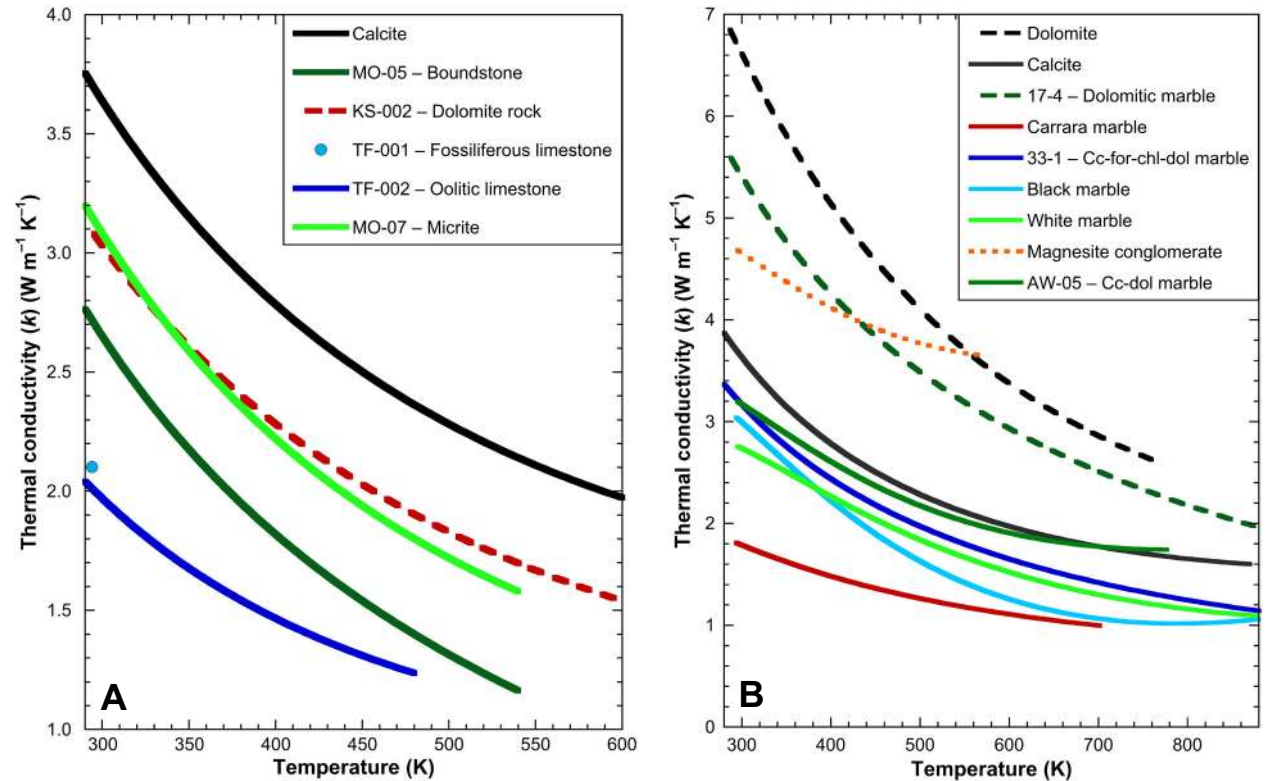
Marble Thermal Conductivity

Thermal conductivity of undeformed Carrara Marble at 294 K (Fig. 10B) was lower than that of any of the limestones at ~1.8 W m^{-1} K^{-1}, but the deformed sample had a higher *k* of ~2.1 W m^{-1} K^{-1} (294 K). This contrast disappeared at elevated temperatures, with the undeformed sample having a *k* of 1.29 W m^{-1} K^{-1} at 484 K and the deformed sample a similar *k* of 1.19 W m^{-1} K^{-1} at 513 K. Threshold marble and Black marble both had *k* in the range of measured limestones as well, but higher than that of the Carrara Marble. Marble 33-1 was the only calcite-dominated marble with room-temperature *k* higher than that of the limestones at 3.17 W m^{-1} K^{-1} (average of all orientations), but contains high-*D* forsterite and dolomite (Table 1).

Unlike sample TF-002 (dolomite rock), dolomite-dominated marble 17-4 strongly reflected the higher *k* of the mineral dolomite with a room-temperature *k* of 5.4 W m^{-1} K^{-1} (300 K, average of four orientations). The decrease in *k* for sample 17-4 was ~45% between 300 K and 600 K. This decrease mirrors that of the mineral dolomite across the same temperature range.

■ DISCUSSION

Controls on Mineral Thermal Diffusivity

Previous LFA measurements have shown that minerals rich in magnesium tend to produce high *D* when compared to isochemical analogs with heavier cations. For example, Pertermann and Hofmeister (2006) reported a room-temperature *D* for pure forsterite in [001] of 5.14 mm^2 s^{-1}, but substitution of 0.005 mole fraction Co for Mg in the same orientation lowered *D* to 4.17 mm^2 s^{-1}, and 0.08 mole fraction Fe for Mg further reduced *D* to 2.60 mm^2 s^{-1} also in [001]. This relationship appears to hold for carbonates (Fig. 11). Magnesite, dolomite, and calcite fall on a linear trend of increasing *D* with decreasing cation mass for group 2 cations. We predict that huntite, a compound carbonate with the formula $Mg_3Ca(CO_3)_4$, thus would have a room-*T* thermal diffusivity of ~3.3 mm^2 s^{-1} if it also follows this trend.

Rhodochrosite does not follow this trend, despite having the same trigonal structure. This suggests that *D* for the other transition-metal trigonal carbon-

Figure 11. (A) Thermal diffusivity (*D*) versus cation mass of minerals at temperatures indicated. Magnesite-dolomite-calcite form a roughly linear trend at all temperatures, but rhodochrosite falls outside of this trend, with higher *D* than the trend would suggest. AMU—atomic mass units. (B) *D* versus unit cell volume. Like for *D* versus cation mass, magnesite-dolomite-calcite form a roughly linear trend, but here rhodochrosite has much lower *D* than this trend would indicate. Values are for room temperature.
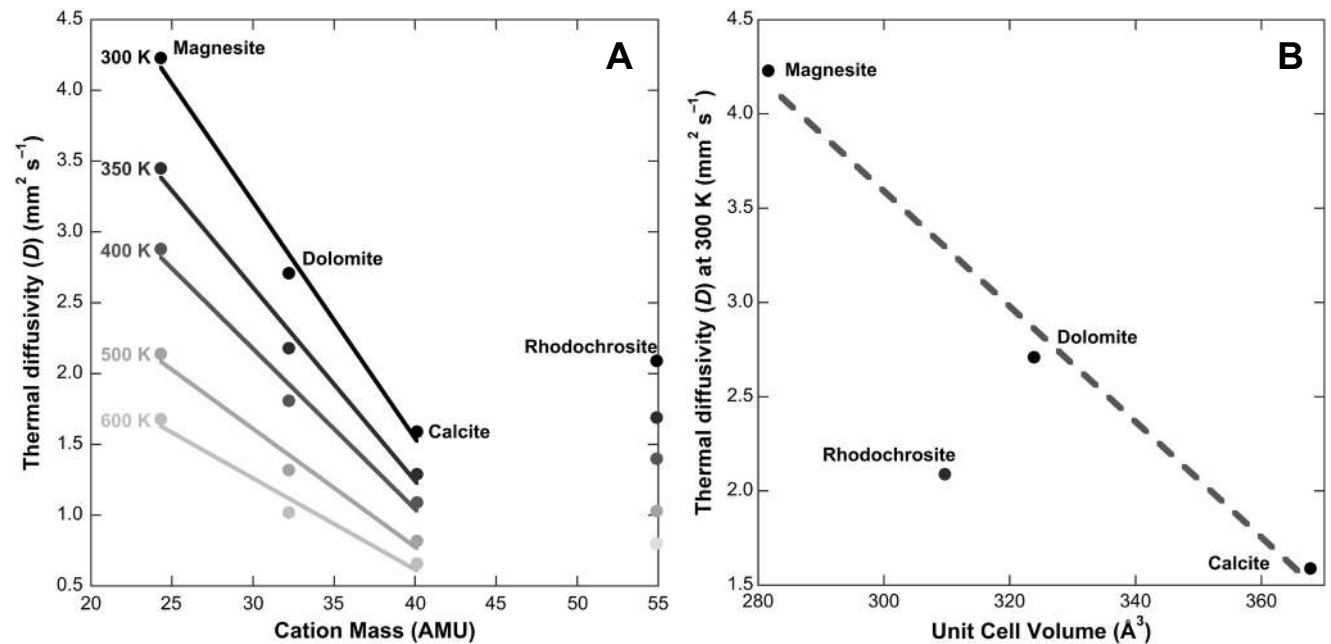
ates (siderite, otavite, smithsonite, sphaerocobaltite, and the compound trigonal carbonate ankerite) cannot be projected from these results using cation mass alone, however we were unable to locate sufficiently pure samples of these minerals to test this hypothesis. A similar pattern is observed when plotting *D* versus unit cell size (Fig. 11B), with *D* increasing with decreasing unit cell size from calcite to dolomite to magnesite, and rhodochrosite similarly plotting off of this trend.

Rock Thermal Diffusivity

Rock thermal diffusivity varies as a function of both mineralogy and texture. Dolomite-dominated rocks reflect the higher *D* of the mineral dolomite across all temperatures measured for similarly textured rocks. For example, Threshold marble, which is dominated by calcite, had a room-temperature *D* of 1.29 mm² s⁻¹, but *D* of dolomitic marble 17-4 was nearly twice that (2.00–2.64 mm² s⁻¹ depending on orientation). Both Threshold marble and marble 17-4 have moderately large grains, clean grain boundaries, and low porosities (<5%). This same effect is reflected in sedimentary rocks, where the dolomite rock KS-002 had a *D* at room *T* of 1.48 mm² s⁻¹, compared to 1.03 mm² s⁻¹ for oolitic limestone (TF-002), despite similar porosities (15% versus 13% respectively).

Several previous studies have explored textural controls on thermal transport properties within carbonate rocks, specifically the effects of porosity (ϕ) on *k*, resulting in theoretical models based on experimental results, statistical analysis, and numerical models of heat flow on a hand-sample scale (e.g., Carson et al., 2005; Çanakci et al., 2007; Yaşar et al., 2008; Alishaev et al., 2012; Fuchs et al., 2013). Carson et al. (2005) proposed two end-member models of effective *k* in which heat flow within the material is through either "internal" porosity or "external" porosity (Fig. 12, where Maxwell-Eucken 1 represents the upper bounds of internal porosity and Maxwell-Eucken 2 the lower bounds of external porosity). In "internal porosity materials", heat flows primarily through the continuous medium surrounding the dispersed phase (in this case, pore spaces), and in "external porosity materials", heat flows through both the continuous phase and dispersed medium, but preferentially takes the pathway through the dispersed phase. The practical repercussions of this are that *k* does not necessarily vary linearly with porosity, and consequently neither does *D*.

Besides porosity, factors affecting *D* can include grain size, distribution of dispersed phases within the rock, and the presence and nature of fluids within pore space. Grain size varied little for the samples in this study. The LFA method requires rocks to be measured "dry", allowing us to focus on mineralogy and porosity. Porosities vary from ~3% to 19% within the suite, and higher porosity correlates with lower bulk-rock *D* (and consequently, *k*; see Fig. 12).
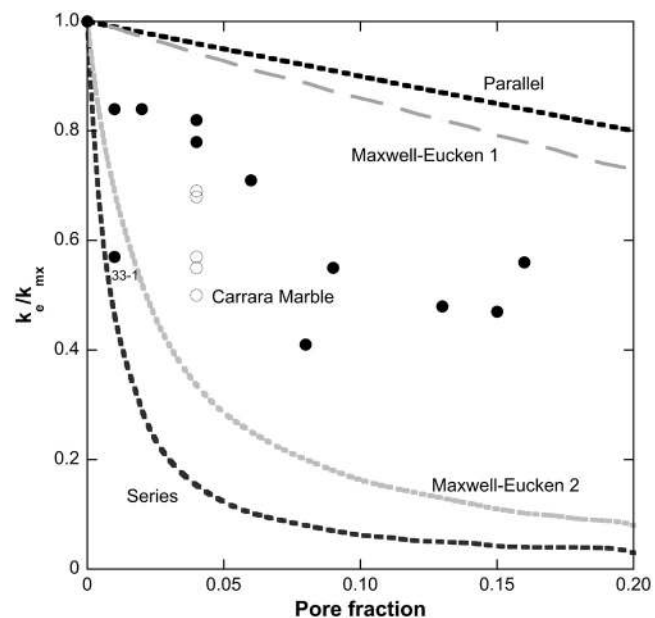
Figure 12. Ratio of effective thermal conductivity (thermal conductivity [k] including pore space, k_e) to matrix thermal conductivity (k calculated from mineral proportions without pore space, k_{mx}) versus pore fraction for samples used in this study. Open circles are Carrara Marble values calculated using measured porosity indicated in Table 1 (porosity for each disk was not available). All samples fall within the boundaries of the Maxwell-Eucken model (where Maxwell-Eucken 1 is the upper limit of internal porosity, and Maxwell-Eucken 2 is the lower limit of external porosity), except for sample 33-1. Parallel and series indicate calculation of k_e using a resistor-in-parallel and resistor-in-series model respectively. All four curves are mixing models wherein pore space is distributed in parallel (heat flows indiscriminately through matrix and pore space and thus is averaged), series (wherein heat must flow through all components in series), and is either a dispersed phase with no connected pore space (Maxwell-Eucken 1), or composes the matrix (Maxwell-Eucken 2). See Carson et al. (2005) for more information.

Sample selection and preparation may influence measured D (or k). For example, Carrara Marble is dominated by calcite and has a low porosity (ϕ = 4%), but had the lowest D of any sample studied here. The sample is brittle to the touch, but contains a more cohesive core when the outer layers are removed. When D was measured for the internal cohesive core, the sample produced higher a higher D (Fig. 8, Run 3 [reground 2×], "Trapezoid"). This has two implications: First, poorly cohesive rocks may be slow conductors even if little pore space is present. Cement between grains may consist of very fine material, which acts as a thermal barrier to conduction (Branlund and Hofmeister, 2008). Second, poorly consolidated rocks could produce anomalously low D or k even if measured with accurate methods because sample cohesion has been compromised during or following depressurization.

Comparison to Silicate Minerals

The thermal diffusivity of carbonate minerals is broadly similar to that of many common silicate minerals. For example, directionally averaged forsterite has a room-T thermal diffusivity of ~2.5 mm² s⁻¹ (Pertermann and Hofmeister, 2006), compared to directionally averaged dolomite of this study (white + grey) at 2.6 mm² s⁻¹. This is significantly lower than the D of directionally averaged quartz (4.9 mm² s⁻¹; Branlund and Hofmeister, 2007), but dD/dT of dolomite is higher than that of forsterite. Near 600 K, dolomite D falls to ~1.1 mm² s⁻¹, where D for directionally averaged quartz is ~1.7 mm² s⁻¹ and for forsterite is ~2 mm² s⁻¹. At the maximum temperature measured for dolomite (898 K), D approaches a limit of ~0.6 mm² s⁻¹, while both forsterite and quartz approach ~1 mm² s⁻¹. Magnesite displays a D that is similar to that of quartz, with D of magnesite of 4.2 mm² s⁻¹ at 300 K, and falling to 1.7 mm² s⁻¹ at 600 K.

Calcite has D values that compare to those of more insulating silicate minerals such as albite (directionally averaged Amelia albite D = 1.36 mm² s⁻¹ at 293 K; Hofmeister et al., 2009), but significantly lower than that of dolomite. Furthermore, calcite D appears to reach a minimum at a much lower temperature and lower values (~0.5 mm² s⁻¹ near 600 K) than that of dolomite. This suggests that, barring textural differences, calcite-dominated rocks should be more insulating than dolomite-, quartz-, or olivine-dominated rocks, and that sedimentary basins dominated by calcite are more insulating than those dominated by dolomite or quartz.

Models of Temperature Dependence in the Literature

Several models have been published that use single-value low-temperature k measurements to model the temperature dependence of k for the rock. This is an attractive concept, as measuring the temperature dependence of k for every rock from a drill-hole core is impractical and expensive. Figures 13A–13C show the results of using several of these models with low T values for rocks from this study to predict the temperature response of k for the sample compared to the calculated k values using measured D, C_P, and ρ.

Although several models produce similar T versus k trends for some samples (e.g., calculated k for sample 33-1 is reproduced by the Chapman et al. [1984] model with <5% error), no model consistently predicts the T dependence of k for the suite of rocks studied here. Thus, using these models to predict k for a sample across temperatures found in the crust would produce moderate to significant error (~5%–125%). This is unsurprising, as these models are calibrated using techniques with systematic errors resulting from contacts and/or ballistic radiative transfer, and commonly do not use equations that have a basis in the physics of diffusive transport. Thus, even an accurate low-T measurement used with one of these models will produce an unpredictable error in calculated elevated-T properties.
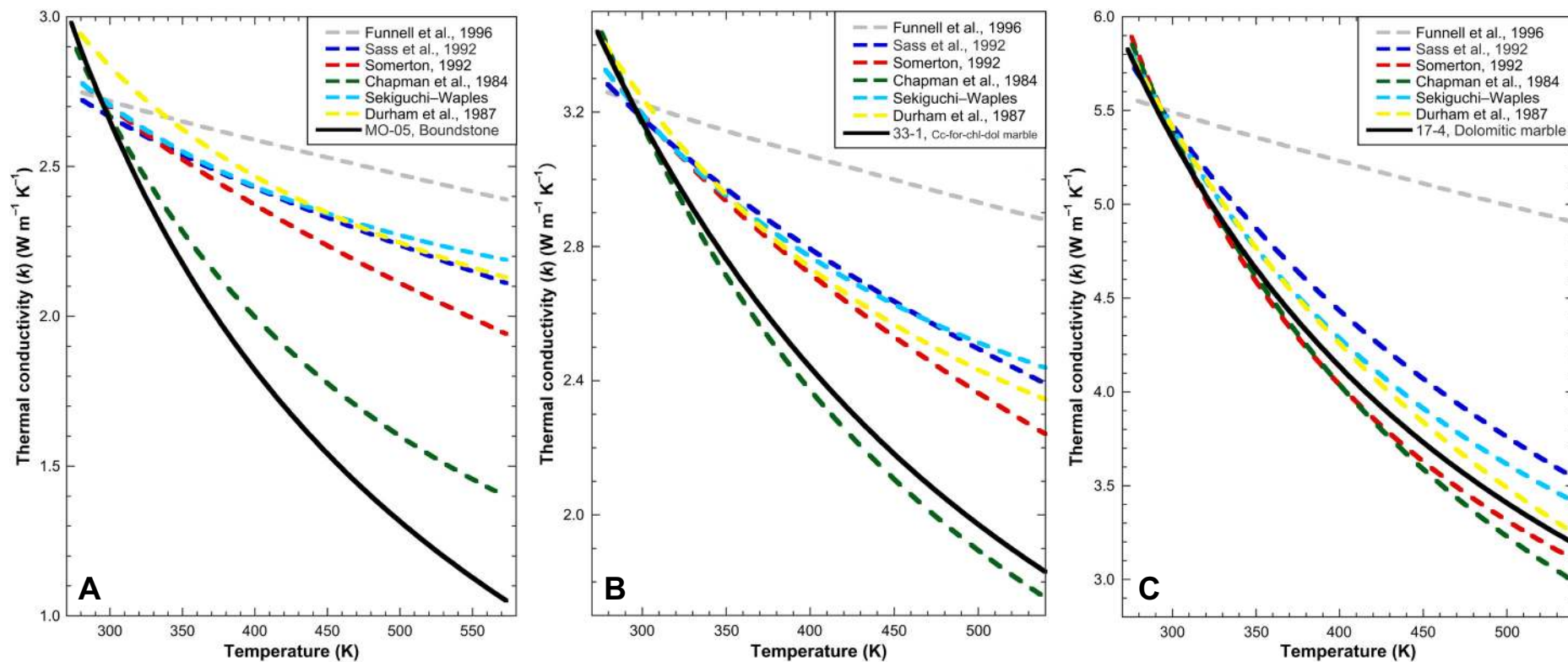
Figure 13. Comparison of temperature-dependent thermal conductivity (k) calculated using measured values of thermal diffusivity (D), isobaric heat capacity (C_p), and density for samples MO-05 (A), 33-1 (B), and 17-4 (C) with models for the temperature dependence of k using single measurements at low temperature. The model of Durham et al. (1987) uses k measured at 273 K, the model of Sass et al. (1992) at 297 K, and all others at 293 K. The Sekiguchi-Waples model is found in Hantschel and Kauerauf (2009). cc—calcite; for—forsterite; chl—chlorite; dol—dolomite.

Implications for Thermal Modeling

The results of this study have several implications for basin modeling, and suggest further lines of enquiry. First, closure of pore space with depth in a basin is predicted to lead to an increase in D and k as recrystallization occurs and low-conductivity pore space and amorphous or organic material are replaced with crystalline grains. This is apparent from the contrast in both D and k between porous limestones TF-002 and MO-05, low-porosity MO-07, and calcite-dominated Threshold marble and Black marble (Figs. 6 and 10A), which persists to elevated temperatures. This result is not a new concept (e.g., Carson et al., 2005), but previous methods used to constrain the effects on porosity have an uncontrolled parameter in the form of experimental error associated with imperfect contacts. Note that pressures attained in the crust are on the order of ~1–1.5 GPa, and because D increases

only ~4% per gigapascal, this effect can be neglected (see introduction and references therein).

Because the results presented here show a stronger temperature dependence and variability for D and k of carbonate rocks than predicted by current models (Fig. 13), the geothermal gradient of crusts with carbonate rocks and the conductive properties that influence it are more strongly coupled. As an example of the interplay of these effects, we present a model of two *ad hoc* crustal columns with 10 km of carbonate rocks in the upper crust as shown in Figure 14, and using input parameters as listed in Table 6. The two model columns differ by the dominant upper-crustal mineral: one is calcite dominated, and one is dolomite dominated. Inputs for thermal diffusivity were chosen to roughly mirror a reduced porosity with depth, with limestones composing the upper 6 km of the calcite-dominated model, and the calcite marble Threshold marble filling out the lower 4 km of the upper crust. By comparison, dolomite
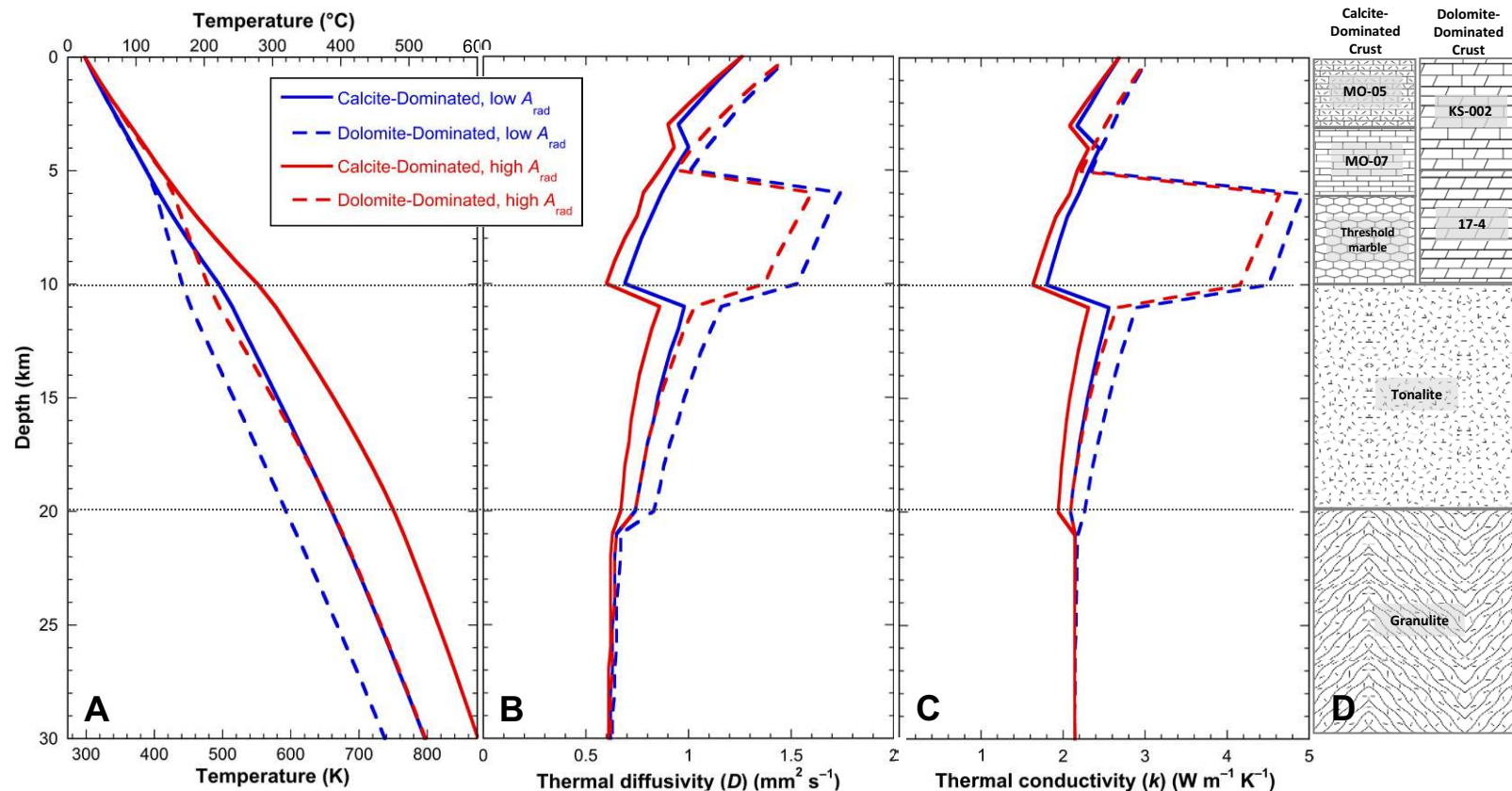
Figure 14. Modeled geothermal gradients (A) showing variability in the geotherm resulting from coupling between thermal diffusivity (D; B) and internal heat production (A_{rad}; Table 6). Heat production is concentrated in the lower tonalite (lower crust) and granite (middle crust). Thermal conductivity (k; C) was calculated from model results for the geothermal gradient and thermal diffusivity. Rock inputs for the crustal structure (D) were chosen to roughly simulate reduced porosity with depth within the "basin" and illustrate the effects of dolomitization on the ability of a basin to conduct heat. All rock inputs are from this paper except tonalite and granodiorite (Merriman et al., 2013). MO-05—boundstone; MO-07—micrite; Threshold marble—pure calcite marble; KS-002—sedimentary dolomite rock; 17-4—dolomitic marble.

rock KS-002 overlies dolomitic marble 17-4 in the dolomite-dominated upper crust. Both crusts are 30 km thick, with a middle 10 km of a high-modal-quartz tonalite and a lower 10 km of granulite (thermal diffusivity values from Merriman et al., 2013).

The finite-difference software package Lithoheat (Nabelek et al., 2010) was used to calculate geothermal gradients and heat fluxes for both model columns. Lithoheat uses boundary conditions of surface temperature (298 K) and basal temperature (1573 K). Constant basal heat flux was not used because it implies temperatures increase (or decrease) in the asthenosphere in response to elevated (or reduced) temperatures at the base of the lithosphere to keep heat flux into the lithosphere constant (Nabelek and Liu, 2004). Heat production within the lithosphere is thus the major driving force behind the thermal

structure of the lithosphere, and in our models was concentrated in the middle tonalite layer, with minor heat production in the granulite layer. Although basins typically contain higher heat production in the upper crust, this is usually concentrated in other rock types such as shales (e.g., Norden and Förster, 2006). Each model column was run to steady state using two different internal heat production (A_{rad}) values by varying the heat production in the tonalite layer (2.38 mW m^{-3} versus 1.19 mW m^{-3}), for a total of four models.

Figure 14 shows the resulting geothermal gradients, thermal diffusivity, and thermal conductivity profiles. Two columns are shown: one with an upper 10 km of calcite-rich rocks (solid lines), and one with an upper 10 km of dolomitized carbonates (dashed lines). The models predict values of D resulting from computed geothermal gradients that vary strongly depending on the tex-

TABLE 6. MODEL PARAMETERS AND HEAT FLUX RESULTS

Model	Upper crust composition and thickness*	Middle crust heat production (mW m^{-3})	Lower crust heat production (mW m^{-3})	Surface heat flux[†] (mW m^{-3})	Asthenospheric heat flux[†] (mW m^{-3})
Calcite dominated, low A_{rad}	Sample MO-05: 3 km Sample MO-07: 3 km Threshold marble: 4 km	1.19	0.42	43.4	24.7
Calcite dominated, high A_{rad}	Sample MO-05: 3 km Sample MO-07: 3 km Threshold marble: 4 km	2.38	0.42	52.4	21.8
Dolomite dominated, low A_{rad}	Sample KS-002: 5 km Sample 17-4: 5 km	1.19	0.42	45.6	26.9
Dolomite dominated, high A_{rad}	Sample KS-002: 5 km Sample 17-4: 5 km	2.38	0.42	55.3	24.7

Note: See text for description of rock type associated with each sample number. Middle crust transport properties are those of tonalite KB12 (Merriman et al., 2013), lower crust properties are those of granite (Whittington et al., 2009). Middle crust thickness = 10 km, lower crust thickness = 10 km. Lithospheric mantle thickness = 90 km. Lower boundary condition = 1300 °C (see text for discussion); upper boundary condition = 25 °C. A_{rad}—volumetric heat production.
  *Upper crust heat production is due to low-heat-producing elements typical of carbonate rocks.
  [†]Heat flux calculated from modeled thermal gradient and thermal conductivity (Equation 1 [see text]).

ture and mineralogy of the different layers. For example, D varied by as much as 0.87 mm^2 s^{-1} between the calcite-dominated crust (0.87 mm^2 s^{-1} at 6 km depth) and the dolomitized crust (1.74 mm^2 s^{-1}). Even within a single layer for identical crustal configurations, the calculated value of D varied by as much as 13%, and the resulting k as much as 10%, because of variations in temperature between hot and cold models. In other words, the geothermal gradient depends on the ability of the rocks to conduct heat, which in turn influences the geotherm. The resulting temperatures vary by as much as 90 K between calcite- and dolomite-dominated models, even when heat production was the same for both crustal columns. Some of these results would be hidden by surface heat flow measurements, as predicted heat flow at the surface is nearly identical for both low-A_{rad} models (43.4 mW m^{-2} for the calcite-dominated crust versus 45.6 mW m^{-2} for the dolomite-dominated crust).

Furthermore, variations in thermal transport properties partially obscure variations in heat production in the crust. This is highlighted by temperatures in the low-A_{rad} calcite-dominated crust versus those in the high-A_{rad} dolomitized crust, where *average* crustal temperatures vary by only <1 K, and *peak* temperature contrasts are a modest 22 K at 5 km depth (410 K for high-A_{rad} dolomitized crust, 388 K for low-A_{rad} calcite-dominated crust).

■ CONCLUSIONS

Multiple properties combine to control thermal diffusivity of both minerals and rocks, the effects of which are more variable at low temperatures. Rock thermal diffusivity is in part controlled by mineralogy, which in carbonate rocks is typically dominated by either generally low-D calcite or higher-D dolomite, with proportions of other common minerals such as quartz or feldspar adding an additional layer of complexity. Mineral D itself is controlled

by mineral structure and cation mass, as well as volume of the unit cell. The composite mineral dolomite has D that is the weighted average of that of calcite and magnesite at all temperatures. The data for rhodochrosite suggest that transition-metal carbonates do not follow the same trend as those with alkaline-earth metals (calcite-dolomite-magnesite), and that properties of other carbonate minerals not studied here (e.g., siderite, smithsonite) cannot be predicted from this trend.

For carbonate rocks, texture is a primary control on bulk-rock D, as porosity generally reduces D across all measured temperatures, but in a nonlinear fashion. Additional textural concerns may include dispersed minor phases such as graphite, sample cohesion, and grain size. The size of the suite measured for this work, however, is insufficient to fully characterize these effects. Metamorphism of sedimentary carbonates may increase bulk-rock D, in part by porosity reduction, which occurs in sedimentary rocks under confining pressure or in the presence of fluids, but also by increasing grain size and replacement of lower-D minerals such as calcite with higher-D minerals such as forsterite.

Composition also has the potential to influence the thermal structure of crust that has a large component of carbonate rocks, as a higher contrast exists between the conductive ability of the minerals calcite and dolomite than previously thought. This contrast exists across all temperatures measured (Figs. 5 and 9), and strongly suggests that basins that have undergone dolomitization will conduct heat more efficiently than those that are dominated by calcite (Fig. 14). All other factors being equal, this suggests that geothermal gradients would be lower in dolomitized basins, and petroleum maturation windows or sources of geothermal energy would be deeper.

Thermal conductivity results presented here suggest that published values of k for both carbonate minerals and carbonate rocks contain systematic errors similar to those found in other mineral and rock groups. This typically results in published values for k using contact methods being lower at low

temperatures and higher at high temperatures than values calculated through the LFA method. These results show that the conductive ability of carbonate regimes is likely more sensitive to local temperature than previously thought, and models using older k data or temperature-dependent models for k based on older data need re-evaluation. This is particularly true for models that incorporate a large temperature gradient over a small distance. For example, Nabelek et al. (2012) modeled emplacement of a granitic pluton into dolomitic marble using T-dependent D. Compared to a model with a fixed D of 1 mm^2 s^{-1}, temperatures in the pluton remained above the solidus more than twice as long because of the feedback between elevated temperatures in the country rock and its ability to diffuse the heat away. An extended residence time provides a longer-lasting thermal engine to drive metamorphic processes such as contact metamorphism or skarn mineralization. Furthermore, models that use a single, low-temperature value of k to predict its change with temperature are based on methods that include significant error, and do not correctly predict the change in k with temperature.

REFERENCES CITED

Aines, R.D., and Rossman, G.R., 1985, The high temperature behavior of trace hydrous components in silicate minerals: The American Mineralogist, v. 70, p. 1169–1179.

Alishaev, M.G., Abdulagatov, I.M., and Abdulagatova, Z.Z., 2012, Effective thermal conductivity of fluid-saturated rocks: Experiment and modeling: Engineering Geology, v. 135–136, p. 24–39, https://doi.org/10.1016/j.enggeo.2012.03.001.

Armstrong, J.T., 1995, CITZAF, a package of correction programs for the quantitative electron microbeam X-ray analysis of thick polished materials, thin films, and particles: Microbeam Analysis, v. 4, p. 177–200.

Avard, G., and Whittington, A.G., 2012, Rheology of arc dacite lavas: Experimental determination at low strain rates: Bulletin of Volcanology, v. 74, p. 1039–1056, https://doi.org/10.1007/s00445-012-0584-2.

Berner, R.A., and Caldeira, K., 1997, The need for mass balance and feedback in the geochemical carbon cycle: Geology, v. 25, p. 955–956, https://doi.org/10.1130/0091-7613(1997)025<0955:TNFMBA>2.3.CO;2.

Bickle, M.J., 1996, Metamorphic decarbonation, silicate weathering, and the long-term carbon cycle: Terra Nova, v. 8, p. 270–276, https://doi.org/10.1111/j.1365-3121.1996.tb00756.x.

Birch, A.F., and Clark, H., 1940, The thermal conductivity of rocks and its dependence upon temperature and composition: American Journal of Science, v. 238, p. 529–558, https://doi.org/10.2475/ajs.238.8.529.

Branlund, J.M., and Hofmeister, A.M., 2007, Thermal diffusivity of quartz to 1,000°C: Effects of impurities and the α-β transition: Physics and Chemistry of Minerals, v. 34, p. 581–595, https://doi.org/10.1007/s00269-007-0173-7.

Branlund, J.M., and Hofmeister, A.M., 2008, Factors affecting heat transfer in natural SiO_2 solids: The American Mineralogist, v. 93, p. 1620–1629, https://doi.org/10.2138/am.2008.2821.

Branlund, J.M., and Hofmeister, A.M., 2012, Heat transfer in plagioclase feldspars: The American Mineralogist, v. 97, p. 1145–1154, https://doi.org/10.2138/am.2012.3986.

Bräuer, H., Dusza, L., and Schulz, B., 1992, New laser flash equipment LFA 427: Interceram, v. 41, p. 489–492.

Çanakci, H., Demirboğa, R., Karakoç, M.B., and Şirin, O., 2007, Thermal conductivity of limestone from Gaziantep (Turkey): Building and Environment, v. 42, p. 1777–1782, https://doi.org/10.1016/j.buildenv.2006.01.011.

Carson, J.K., Lovatt, S.J., Tanner, D.J., and Cleland, A.C., 2005, Thermal conductivity bounds for isotropic, porous materials: International Journal of Heat and Mass Transfer, v. 48, p. 2150–2158, https://doi.org/10.1016/j.ijheatmasstransfer.2004.12.032.

Chapman, D.S., Keho, T.H., Bauer, M.S., and Picard, M.D., 1984, Heat flow in the Uinta Basin determined from bottom hole temperature (BHT) data: Geophysics, v. 49, p. 453–466, https://doi.org/10.1190/1.1441680.

Clauser, C., and Huenges, E., 1995, Thermal conductivity of rocks and minerals, in Ahrens, T.J., ed., Rock Physics and Phase Relations: A Handbook of Physical Constants, American Geophysical Union Reference Shelf 3, p. 105–126, https://doi.org/10.1029/RF003p0105.

Cowan, D.R., 1963, Pulse method of measuring thermal diffusivity at high temperatures: Journal of Applied Physics, v. 34, p. 926–927, https://doi.org/10.1063/1.1729564.

Criss, E.M., and Hofmeister, A.M., 2017, Isolating lattice from electronic contributions in thermal transport measurements of metals and alloys and a new model: International Journal of Modern Physics B, v. 31, 175020, https://doi.org/10.1142/S0217979217502058.

Deer, W.A., Howie, R.A., and Zussman, J., 1992, An Introduction to the Rock-Forming Minerals (second edition): Harlow, Essex, Pearson Education Limited, 696 p.

Durham, W.B., Mirkovich, V.V., and Heard, H.C., 1987, Thermal diffusivity of igneous rocks at elevated pressure and temperature: Journal of Geophysical Research, v. 92, p. 11,615–11,634, https://doi.org/10.1029/JB092iB11p11615.

Fei, Y., 1995, Thermal expansion, in Ahrens, T.J., ed., Mineral Physics and Crystallography: A Handbook of Physical Constants: Washington, DC, American Geophysical Union, p. 29–44, https://doi.org/10.1029/RF002p0029.

Fuchs, S., Schütz, F., Förster, H.-J., and Förster, A., 2013, Evaluation of common mixing models for calculating bulk thermal conductivity of sedimentary rocks: Correction charts and new conversion equations: Geothermics, v. 47, p. 40–52, https://doi.org/10.1016/j.geothermics.2013.02.002.

Funnell, R., Chapman, D., Allis, R., and Armstrong, P., 1996, Thermal state of the Taranaki Basin, New Zealand: Journal of Geophysical Research, v. 101, p. 25,197–25,215, https://doi.org/10.1029/96JB01341.

Gratz, K., 2006, Über den Wärmetransport in Karbonaten [Ph.D. thesis]: Potsdam, Freie Universität Berlin, 95 p.

Hantschel, T., and Kauerauf, A.I., 2009, Fundamentals of Basin and Petroleum Systems Modeling: Dordrecht, Springer, 475 p.

He, M., Su, C., Liu, X., Qi, X., and Lv, N., 2015, Measurement of isobaric heat capacity of pure water up to supercritical conditions: The Journal of Supercritical Fluids, v. 100, p. 1–6, https://doi.org/10.1016/j.supflu.2015.02.007.

Henderson, J.B., Hagemann, L., and Blumm, J., 1998a, Development of SRM 8420 series electrolytic iron a thermal diffusivity standard: Netzsch Applications Laboratory Thermophysical Properties Section Report I-9E, 11 p.

Henderson, J.B., Giblin, F., Blumm, J., and Hagemann, L., 1998b, SRM 1460 series as a thermal diffusivity standard for laser flash instruments: International Journal of Thermophysics, v. 19, p. 1647–1656, https://doi.org/10.1007/BF03344916.

Hofmeister, A.M., 2006, Thermal diffusivity of garnets at high temperature: Physics and Chemistry of Minerals, v. 33, p. 45–62, https://doi.org/10.1007/s00269-005-0056-8.

Hofmeister, A.M., 2007, Pressure dependence of thermal transport properties: Proceedings of the National Academy of Sciences of the United States of America, v. 104, p. 9192–9197, https://doi.org/10.1073/pnas.0610734104.

Hofmeister, A.M., 2010, Scale aspects of heat transport in the diamond anvil cell, in spectroscopic modeling, and in Earth's mantle: Implications for secular cooling: Physics of the Earth and Planetary Interiors, v. 180, p. 138–147, https://doi.org/10.1016/j.pepi.2009.12.006.

Hofmeister, A.M., and Branlund, J.M., 2015, Thermal conductivity of the Earth, in Schubert, G., Price, G.D., and Stixrude, L., eds., Treatise on Geophysics (second edition), Volume 2: Mineral Physics: Elsevier, Amsterdam, p. 583–608, https://doi.org/10.1016/B978-0-444-53802-4.00047-6.

Hofmeister, A.M., and Perterman, M., 2008, Thermal diffusivity of clinopyroxenes at elevated temperature: European Journal of Mineralogy, v. 20, p. 537–549.

Hofmeister, A.M., Pertermann, M., and Branlund, J.M., 2007, Thermal conductivity of the Earth, *in* Price, G.D., ed., Treatise on Geophysics, Volume 2: Mineral Physics: Amsterdam, The Netherlands, Elsevier, p. 543–577, https://doi.org/10.1016/B978-044452748-6.00048-1.

Hofmeister, A.M., Whittington, A.G., and Pertermann, M., 2009, Transport properties of high albite crystals, near-endmember feldspar and pyroxene glasses, and their melts to high temperature: Contributions to Mineralogy and Petrology, v. 158, p. 381–400, https://doi.org/10.1007/s00410-009-0388-3.

Hofmeister, A.M., Dong, J., and Branlund, J.M., 2014, Thermal diffusivity of electrical insulators at high temperatures: Evidence for diffusion of bulk phonon-polaritons at infrared frequencies augmenting phonon heat conduction: Journal of Applied Physics, v. 115, 163517, https://doi.org/10.1063/1.4873295.

Horai, K.-i., 1971, The thermal conductivity of rock-forming minerals: Journal of Geophysical Research, v. 76, p. 1278–1308, https://doi.org/10.1029/JB076i005p01278.

Hust, J.G., and Lankford, A.B., 1984, Update of thermal conductivity and electrical resistivity of electrolytic iron, tungsten, and stainless steel: National Bureau of Standards Special Publication 260-90, 71 p.

Jacobs, G.K., Kerrick, D.M., and Krupka, K.M., 1981, The high-temperature heat capacity of natural calcite ($CaCO_3$): Physics and Chemistry of Minerals, v. 7, p. 55–59.

Krupka, K.M., Hemingway, B.S., Robie, R.A., and Kerrick, D.M., 1985, High-temperature heat capacities and derived thermodynamic properties of anthophyllite, diopside, dolomite, enstatite, bronzite, talc, tremolite, and wollastonite: The American Mineralogist, v. 70, p. 261–271.

Lee, Y., and Deming, D., 1998, Evaluation of thermal conductivity temperature corrections applied in terrestrial heat flow studies: Journal of Geophysical Research, v. 103, p. 2447–2454, https://doi.org/10.1029/97JB03104.

Lippmann, F., 1973, Sedimentary Carbonate Minerals: New York, Springer-Verlag, 228 p., https://doi.org/10.1007/978-3-642-65474-9.

Liu, S., Feng, C., Wang, L., and Li, C., 2011, Measurement and analysis of thermal conductivity of rocks in the Tarim Basin, northwest China: Acta Geologica Sinica, v. 85, p. 598–609, https://doi.org/10.1111/j.1755-6724.2011.00454.x.

Maglić, K.D., and Taylor, R.E., 1992, The apparatus for thermal diffusivity measurement by the laser pulse method, *in* Maglić, K.D., Cezairliyan, A., and Peletsky, V.E., eds., Compendium of Thermophysical Property Measurement Methods, Volume 2: Recommended Measurement Techniques and Practices: New York, Plenum Press, p. 281–314, https://doi.org/10.1007/978-1-4615-3286-6_10.

Mehling, H., Hautzinger, G., Nilsson, O., Fricke, J., Hofmann, R., and Hahn, O., 1998, Thermal diffusivity of semitransparent materials determined by the laser-flash method applying a new mathematical model: International Journal of Thermophysics, v. 19, p. 941–949, https://doi.org/10.1023/A:1022611527321.

Merriman, J.D., Whittington, A.G., Hofmeister, A.M., Nabelek, P.I., and Benn, K., 2013, Thermal transport properties of major Archean rock types to high temperature and implications for cratonic geotherms: Precambrian Research, v. 233, p. 358–372, https://doi.org/10.1016/j.precamres.2013.05.009.

Miao, S.Q., Li, H.P., and Chen, G., 2014, Temperature dependence of thermal diffusivity, specific heat capacity, and thermal conductivity for several types of rocks: Journal of Thermal Analysis and Calorimetry, v. 115, p. 1057–1063, https://doi.org/10.1007/s10973-013-3427-2.

Moore, G.E., 1943, Heat content of manganese dioxide and carbonate at high temperatures: Journal of the American Chemical Society, v. 65, p. 1398–1399, https://doi.org/10.1021/ja01247a034.

Nabelek, P.I., and Liu, M., 2004, Petrologic and thermal constraints on the origin of leucogranites in collisional orogens: Transactions of the Royal Society of Edinburgh: Earth Sciences, v. 95, p. 73–85, https://doi.org/10.1017/S0263593300000936.

Nabelek, P.I., and Morgan, S.S., 2012, Metamorphism and fluid flow in the contact aureole of the Eureka Valley–Joshua Flat–Beer Creek pluton, California: Geological Society of America Bulletin, v. 124, p. 228–239, https://doi.org/10.1130/B30425.1.

Nabelek, P.I., Whittington, A.G., and Hofmeister, A.M., 2010, Strain heating as a mechanism for partial melting and ultrahigh temperature metamorphism in convergent orogens: Implications of temperature-dependent thermal diffusivity and rheology: Journal of Geophysical Research, v. 115, B12417, https://doi.org/10.1029/2010JB007727.

Nabelek, P.I., Hofmeister, A.M., and Whittington, A.G., 2012, The influence of temperature-dependent thermal diffusivity on the conductive cooling rates and temperature-time paths in contact aureoles: Earth and Planetary Science Letters, v. 317–318, p. 157–164, https://doi.org/10.1016/j.epsl.2011.09.009.

Norden, B., and Förster, A., 2006, Thermal conductivity and radiogenic heat production of sedimentary and magmatic rocks in the Northeast German Basin: American Association of Petroleum Geologists Bulletin, v. 90, p. 939–962, https://doi.org/10.1306/01250605100.

Parker, J.W., Jenkins, J.R., Butler, P.C., and Abbott, G.L., 1961, Flash method of determining thermal diffusivity, heat capacity, and thermal conductivity: Journal of Applied Physics, v. 32, p. 1679–1684, https://doi.org/10.1063/1.1728417.

Pertermann, M., and Hofmeister, A.M., 2006, Thermal diffusivity of olivine-group minerals at high temperature: The American Mineralogist, v. 91, p. 1747–1760, https://doi.org/10.2138/am.2006.2105.

Pertermann, M., Whittington, A.G., Hofmeister, A.M., Spera, F.J., and Zayak, J., 2008, Transport properties of low-sanidine single-crystals, glasses and melts at high temperature: Contributions to Mineralogy and Petrology, v. 155, p. 689–702, https://doi.org/10.1007/s00410-007-0265-x.

Ramachandran, E., Raji, P., Ramachandran, K., and Natarajan, S., 2006, Photoacoustic study of the thermal properties of calcium carbonate—The major constituent of pancreatic calculi: Crystal Research and Technology, v. 41, p. 64–67, https://doi.org/10.1002/crat.200410531.

Rietveld, H.M., 1968, A profile refinement method for nuclear and magnetic structures: Journal of Applied Crystallography, v. 2, p. 65–71, https://doi.org/10.1107/S0021889869006558.

Robie, R.A., and Hemingway, B.S., 1994, Heat capacities of synthetic grossular ($Ca_3Al_2Si_3O_{12}$), macrocrystals of magnesite (($Mg_{0.991}Fe_{0.005}Ca_{0.003}Mn_{0.001})CO_3$), high-temperature superconductors $YBa_2Cu_3O_{6+x}$ and $BiCaSrCu_2O_{6+x}$, and type 321 stainless steel: U.S. Geological Survey Open-File Report 94-223, 12 p.

Robie, R.A., and Hemingway, B.S., 1995, Thermodynamic properties of minerals and related substances at 298.15 K and 1 bar (10^5 pascals) pressure and at higher temperature: U.S. Geological Survey Bulletin 2131, 470 p.

Ronov, A.B., and Yaroshevsky, A.A., 1976, A new model for the chemical structure of the Earth's crust: Geokhimiya, v. 12, p. 1761–1795.

Rossman, G.R., 1988a, Vibrational spectroscopy of hydrous components: Reviews in Mineralogy, v. 18, p. 193–206.

Rossman, G.R., 1988b, Optical spectroscopy: Reviews in Mineralogy, v. 18, p. 207–254.

Rudnick, R.L., and Gao, S., 2003, Composition of the continental crust, *in* Rudnick, R.L., ed., Treatise on Geochemistry, Volume 3: The Crust: Amsterdam, Elsevier, p. 1–64, https://doi.org/10.1016/B0-08-043751-6/03016-4.

Sass, J.H., Lachenbruch, A.H., Moses, T.H., Jr., and Morgan, P., 1992, Heat flow from a scientific research well at Cajon Pass, California: Journal of Geophysical Research, v. 97, p. 5017–5030, https://doi.org/10.1029/91JB01504.

Schütz, F., Norden, B., Förster, A., and the DESIRE Group, 2012, Thermal properties of sediments in southern Israel: A comprehensive data set for heat flow and geothermal energy studies: Basin Research, v. 24, p. 357–376, https://doi.org/10.1111/j.1365-2117.2011.00529.x.

Smith, D.S., Fayette, S., Grandjean, S., Martin, C., Telle, R., and Tonnessen, T. 2003, Thermal resistance of grain boundaries in alumina ceramics and refractories: Journal of the American Ceramic Society, v. 86, p. 105–111, https://doi.org/10.1111/j.1151-2916.2003.tb03285.x.

Somerton, W.H., 1992, Thermal Properties and Temperature-Related Behavior of Rock/Fluid Systems: New York, Elsevier, 257 p.

Vozár, L., and Hohenauer, W., 2003, Flash method of measuring the thermal diffusivity: A review: High Temperatures–High Pressures, v. 35–36, p. 253, https://doi.org/10.1068/htjr119.

Vozár, L., and Hohenauer, W., 2005, Uncertainty of thermal diffusivity measurements using the laser flash method: International Journal of Thermophysics, v. 26, p. 1899–1915, https://doi.org/10.1007/s10765-005-8604-5.

Waples, D.W., and Waples, J.S., 2004, A review and evaluation of specific heat capacities of rocks, minerals, and subsurface fluids; Part 2: Fluids and porous rocks: Natural Resources Research, v. 13, p. 123–130, https://doi.org/10.1023/B:NARR.0000032648.15016.49.

Whittington, A.G., Hofmeister, A.M., and Nabelek, P.I., 2009, Temperature-dependent thermal diffusivity of Earth's crust: Implications for crustal anatexis: Nature, v. 458, p. 319–321, https://doi.org/10.1038/nature07818.

Xu, L., and Evans, B., 2010, Strain heterogeneity in deformed Carrara marble using a microscale strain mapping technique: Journal of Geophysical Research, v. 115, B04202, https://doi.org/10.1029/2009JB006458.

Yaşar, E., Erdoğan, Y., and Güneyli, H., 2008, Determination of thermal conductivity from physico-mechanical properties: Bulletin of Engineering Geology and the Environment, v. 67, p. 219–225, https://doi.org/10.1007/s10064-008-0126-5.